DNA uptake by cell wall-deficient bacteria reveals a putative ancient macromolecule uptake mechanism

Renée Kapteijn[1], Shraddha Shitut[1], Dennis Aschmann[2], Le Zhang[1], Marit de Beer[3], Deniz Daviran[3], Rona Roverts[3], Anat Akiva[3], Gilles P. van Wezel[1,*], Alexander Kros[2], Dennis Claessen[1, 4,*]

[1]Molecular Biotechnology, Institute of Biology, Leiden University, Sylviusweg 72, 2333 BE Leiden, The Netherlands.

[2]Department of Supramolecular and Biomaterials Chemistry, Leiden Institute of Chemistry, Leiden University, Einsteinweg 55, 2333 CC Leiden, The Netherlands

[3]Electron Microscopy Center, Radboudumc Technology Center Microscopy, Nijmegen, The Netherlands

[4]Lead contact

*Correspondence:

G.Wezel@biology.leidenuniv.nl (G.P.v.W.), D.Claessen@biology.leidenuniv.nl (D.C,)

Keywords: cell wall-deficiency; natural transformation; L-forms; endocytosis; horizontal gene transfer; cryo FIB-SEM

SUMMARY

Horizontal gene transfer in bacteria is widely believed to occur via three main mechanisms: conjugation, transduction and transformation. These mechanisms facilitate the passage of DNA across the protective cell wall using sophisticated machinery. We present here a new mechanism of DNA uptake that is independent of canonical DNA uptake machineries and is used by bacteria that live without a cell wall. We show that the cell wall-deficient bacteria engulf extracellular material, whereby intracellular vesicles are formed, and DNA is internalized. This mechanism is not specific to DNA, and allows uptake of other macromolecules and even 125 nm lipid nanoparticles (LNPs). Uptake was prevented by molecules known to inhibit eukaryotic endocytosis, suggesting this to be an energy-dependent process. Given that cell wall-deficient bacteria are considered a model for early life forms, our work provides a possible mechanism for primordial cells to acquire new genetic material or food before invention of the bacterial cell wall.

INTRODUCTION

Bacteria are constantly exposed to changing environmental conditions and rely on their cell envelope for protection. The cell envelope consists of a cell membrane and a cell wall to separate the internal from the external environment. The cell membrane is a phospholipid bilayer that encloses the cytoplasm and functions as a selective barrier. The cell wall consists of a thick peptidoglycan (PG) layer for Gram-positive bacteria and a thinner PG layer surrounded by an outer membrane for Gram-negative bacteria. The peptidoglycan layer is an important mesh-like structure that not only provides protection against mechanical stress and turgor pressure, but also defines cell shape and rigidity.

To facilitate the selective passage of macromolecules across the cell envelope, bacteria have evolved specialized and sophisticated transport systems (Costa et al., 2015; Forster and Marquis, 2012). For instance, naturally transformable bacteria rely on protein complexes for DNA uptake, with components similar to type IV pili or type II secretion systems. Active transport of DNA across the cell wall is facilitated by the retraction of pilus structures that bind DNA (Chen and Dubnau, 2004; Ellison et al., 2018). Alternatively, the assembly and release of short pilus structures are thought to create transient holes in the PG layer that allow DNA to diffuse to the cell membrane (Muschiol et al., 2015). DNA binding and pore-forming proteins are then used to translocate the DNA across the cell membrane.

Although the cell wall is a vital structure for most bacteria, some bacteria naturally lack a cell wall, or can shed their wall under specific conditions. Examples include the members of the Mollicutes, that are parasitic and live in specific osmotically protective environments such as human mucosal surfaces or the phloem sieve tubes of plants (Stülke et al., 2009). Prolonged exposure to environmental stressors such as cell wall-targeting agents generates so-called L-forms, which are cells that proliferate without their cell wall. Reproduction of L-forms is driven by the upregulation of membrane synthesis and is characterized by blebbing, tubulation and

vesiculation (Mercier et al., 2013; Ramijan et al., 2018). These primitive cell-like characteristics make L-forms an attractive model system to study the evolution of early life (Briers et al., 2012b; Errington et al., 2016). How the absence of the cell wall affects uptake of macromolecules such as DNA from the environment is unknown.

In this study we show that L-forms of the filamentous actinomycete *Kitasatospora viridifaciens* can naturally take up DNA independent of the canonical DNA translocation machinery. Instead, uptake is facilitated by a new mechanism of horizontal gene transfer that involves the invagination of the cell membrane leading to internal vesicle formation. Furthermore we show that this mechanism is robust and allows the non-specific uptake of other macromolecules from the environment as well. Given that L-forms are considered a model for early cellular life, our work provides insight into how such ancient cells may have acquired large biomolecules and nanoparticles from the environment without the need for complex transport machineries.

RESULTS

Natural and artificial DNA uptake by wall-deficient cells

K. viridifaciens is a mycelium-forming bacterium that can extrude temporary wall-deficient cells, called S-cells, under conditions of osmotic stress (Ramijan et al., 2018). These cells can only proliferate by rebuilding the cell wall and reverting to a mycelial mode-of-growth, similar to artificially created cell-wall deficient protoplasts. Prolonged incubation of S-cells in high osmotic pressure can induce the switch to an L-form state that allows reproduction without rebuilding the cell wall. It is unknown whether these cell wall-deficient cells can take up DNA via natural transformation. To analyse this, protoplasts, S-cells and L-forms (*alpha*) were incubated with plasmid DNA, and subsequently plated on selective and non-selective medium (Figure 1A). Notably, L-forms were consistently able to take up DNA, unlike protoplasts or S-cells (Figure 1B). This DNA uptake ability was not restricted to the penicillin-induced L-forms (lines *alpha* and *delta*), as the osmotically induced L-form (line M1) (Ramijan et al., 2018) could also take up plasmid DNA. No transformants were obtained with *alpha* when intact or fragmented genomic DNA was used (Figure S1A). While natural transformation was restricted to L-forms, all wall-deficient cells could be chemically transformed using polyethylene glycol (PEG), with protoplasts, S-cells and L-forms having an average transformation efficiency between 1.7 – 2.5% (Figure S1B). The addition of PEG also enabled transformation of *alpha* with genomic DNA, even if this was present in a crude cell extract. On the other hand, use of methylated DNA prevented transformation, indicating that transformation is possible with different types of DNA, but can be limited by the presence of a different methylation pattern (Figure S1C). By contrast, walled cells could not be transformed either with or without PEG (Figure 1B and Figure S1B). These results show that proliferating wall-deficient L-forms can take up DNA naturally, while walled cells and transient wall-deficient S-cells and protoplasts cannot.

L-forms take up DNA in the absence of canonical DNA translocation machinery

Naturally transformable bacteria use a specialized DNA translocation machinery with similarities to type IV pili or type II secretion systems to take up external DNA (Chen and Dubnau, 2004). Similar components of this canonical system might also be involved in DNA uptake by L-forms. A BlastP search using the DNA-binding protein ComEA and channel protein ComEC of the naturally transformable bacterium *Bacillus subtilis* against *K. viridifaciens* yielded two significant hits: BOQ63_29625 (helix-hairpin-helix domain-containing protein) and BOQ63_29630 (ComEC/Rec2 family competence protein), respectively (Figure 1C and Table S1). The *B. subtilis* helicase/DNA translocase ComFA resulted in a hit to a putative Mfd-encoding gene (BOQ63_20315), a widely conserved bacterial protein that mediates transcription-coupled DNA repair (Roberts and Park, 2004). No other orthologues were found that correlated to proteins involved in DNA transport across the cell envelope for *B. subtilis*, the Gram-negative *Neisseria gonorrhoeae* (Kruger and Stingl, 2011) or for the T4SS-related DNA uptake system of *Helicobacter pylori* (Gilbreath et al., 2011) (Table S1). L-forms lack an intact peptidoglycan-based cell wall and therefore DNA must only cross the cell membrane for internalization. As ComEA and ComEC function in DNA transport across the cell membrane (Friedrich et al., 2001; Inamine and Dubnau, 1995; Kruger and Stingl, 2011) we wondered whether these proteins are involved in DNA uptake in L-forms. Therefore, we replaced the putative *comEC* and *comEA* genes in the L-form strain *alpha* by an apramycin resistance cassette (Figure S1D). Strikingly, the simultaneous deletion of the *comEA* and *comEC* genes did not affect the natural transformation efficiency (two-tailed independent t-test, $t(8)=1.572$, $P=0.155$), indicating that DNA uptake by L-forms occurs independent of this canonical DNA translocation machinery (Figure 1D).

High membrane fluidity is not sufficient for natural DNA uptake in wall-deficient cells

One of the factors controlling the development of competence for DNA uptake in *B. subtilis* is the growth phase (Dubnau, 1991; Hamoen et al., 2003). To study if culture age is also affecting the DNA uptake ability of L-forms, differently aged cultures were subjected to a natural transformation assay. One-day old cultures of *alpha* take up DNA more easily than 3- or 7-day old cultures (one-way ANOVA, F (2,9) = 12.16, Tukey post-hoc test, P =.006 and .005 respectively) (Figure 1E). It is not unlikely that differences in membrane properties that occur during cellular growth may in turn affect the DNA uptake ability. Membrane fluidity is a measure for the average viscosity of the lipid bilayer, which can affect the positioning and movement of proteins and lipids within the membrane (Lenaz, 1987). A higher membrane fluidity is characterized by increased fatty acid disorder, lower lipid packing and higher diffusion rates, which can lead to increased membrane permeabilization (Chapman, 1975; Lande et al., 1995). Analysis of the membrane fluidity of the differently aged cultures indicated that the increased DNA uptake ability may correlate positively with the fluidity of the membrane, as deduced from the generalized polarization (GP) (Scheinpflug et al., 2017) (Figure 1F), although no statistical significant differences were observed (Welch ANOVA, F(2, 2.798), with Games-Howell post-hoc test: 1-3 day P = .068; 1-7 day P= 0.134; 3-7 day P = 0.711). A relatively low fluidity might explain why temporary wall-deficient protoplasts and S-cells cannot take up DNA naturally. However, the fluidity of protoplasts was within the range of 1- to 7-day-old cultures as measured using a plate assay (Figure S1E). Subsequent analysis of the GP by fluorescence microscopy imaging showed that although protoplasts and S-cells tend to have less fluid membranes, these values stay within the range of the membrane fluidity of 1- to 7-day old L-forms (Figure S1F). Therefore, although membrane fluidity may contribute to efficient DNA uptake, it is not sufficient to explain this process.

L-forms take up DNA via an endocytosis-like mechanism

To further investigate the mechanism facilitating DNA uptake by L-forms, we added Cy5-labelled plasmid DNA to L-forms expressing cytosolic eGFP. Labelled plasmid DNA was found either on the outside of the L-form cell membrane, or within apparent internal vesicles (Figure 2A and control Figure S2A). As these internal vesicles were devoid of eGFP, we reasoned that they could have originated by an invagination process of the membrane, whereby extracellular material becomes trapped inside the vesicles. To test this directly, we incubated eGFP-expressing L-forms with the fluorescent dye SynapseRed C2M (SynapseRed). Given that SynapseRed cannot diffuse through the cell membrane, any fluorescent signal on the membranes surrounding internal vesicles would be a strong argument that such vesicles were derived from the cell membrane. Indeed, SynapseRed was found to not only stain the cell membrane of the L-forms but also the membranes of internal vesicles after overnight incubation (Figure 2B). Staining with SYTO-9 further indicated that chromosomal DNA was present in the cytosol but not inside internal vesicles (Figure S2B). Incubation of protoplasts producing cytosolic eGFP with Synapse Red showed that areas with less cytosolic fluorescence emission were caused by internal membrane structures rather than by formation of internal vesicles (Figure S2C). Similar incubation of S-cells showed the presence of internal vesicle-like structures. However, unlike for L-forms, subsequent staining of S-cells of a strain producing cytosolic-mCherry with SYTO-9 indicated that these vesicles were filled with chromosomal DNA. This indicates that internal structures observed in protoplasts and S-cells are not the same internal vesicles as those seen in L-forms and may not be involved uptake of external fluids. Taken together, these results strongly suggest that the observed vesicles inside L-forms originate from invagination of the cell membrane whereby extracellular material may become trapped inside such vesicles.

In eukaryotes, endocytosis is a process that enables the uptake of external cargo via internal vesicle formation, which is eventually degraded or recycled (Cossart and Helenius, 2014; Elkin et al., 2016). Fluorescently labelled dextrans are widely used as markers for endocytosis in eukaryotes (Araki et al., 1996; Li et al., 2015). To identify if such an endocytosis-like process could be present in L-forms and to visualize the uptake of external materials, we incubated the cells with Dextran Texas-Red (D-TR) and performed time-lapse imaging. The L-form strain used also expresses DivIVA-eGFP, which has strong affinity for negatively curved membrane regions (*alpha* pKR2) (Hammond et al., 2019; Jurasek et al., 2020). Such regions are expected to be formed upon invagination of the membrane. After 290 minutes of incubation, D-TR was visible inside the L-form and faint spots of DivIVA-eGFP started to appear adjacent to this region (Figure 2C and Video S1). This progressed to a clear inward bulging of the cell membrane with two foci of DivIVA-eGFP on either side of the invaginated membrane and an inflow of D-TR (t=560 min). After 640 min an internal vesicle was formed that contained D-TR. In other cells, DivIVA-eGFP appeared to form a ring-like structure, which sometimes enveloped the invaginating membrane (Figure 2D cell 1 and 2 respectively). The presence of DivIVA near the site of invagination implies the presence of negatively curved regions in the membrane. Notably, DivIVA is not required for vesicle formation or DNA uptake, as the deletion of *divIVA* in *alpha* (*alpha*ΔDivIVA) had no effect on natural transformation (two-tailed independent t-test, $t(8)=0.489$, $P=0.638$) (Figure S2D), and internal vesicles were still formed by this strain (Figure S2E). Furthermore, internalization of D-TR was also observed in L-forms that did not express DivIVA-eGFP, indicating that uptake is not a consequence of the presence of the fusion protein (Figure S2F). Incubation of protoplasts and S-cells with D-TR up to 72 h did not result in D-TR encapsulation in internal vesicles (Figure S2G). Altogether, these results show that the invagination of the cell

195 membrane of L-forms can lead to internal vesicle formation and may represent an endocytosis-
196 like mechanism allowing uptake of molecules, including DNA, from the environment.
197
198 **Lipid nanoparticles are internalized in vesicles in an energy-dependent manner**
199 Lipid nanoparticles (LNPs) are non-viral particles that are used to deliver nucleic acids and
200 drugs to human cells via endocytosis (Cullis and Hope, 2017). LNPs do not have a lipid bilayer
201 structure, but consist of an electron-dense, hydrophobic core of lipids that encapsulate nucleic
202 acids by electrostatic interactions and are surrounded by a layer of PEG-lipids (Cullis and
203 Hope, 2017; Evers et al., 2018; Hou et al., 2021). Once the endosome acidifies the ionizable
204 lipids become positively charged, which allows the LNP to destabilize the endosome
205 membrane and deliver its cargo into the cell. LNPs can also be fluorescently tagged by the
206 incorporation of fluorophore-conjugated phospholipids (Kulkarni et al., 2019). To further
207 explore the ability of L-forms to take up external particles, the cells were incubated with
208 rhodamine-labelled LNPs (LNP-LR, containing 18:1 Liss Rhod PE) with an average size of
209 125 nm to allow their detection inside L-forms. After addition of LNP-LR to 7-day-old L-
210 forms, clear foci could be detected inside the cells after overnight incubation, as well as
211 localization of LNPs to the cell membrane (Figure 3A and Figure S3B and S3C). When L-
212 forms were used that express eGFP in the cytosol, vesicles only contained LNPs and not eGFP,
213 strongly suggesting that the LNPs had been internalized in vesicles devoid of the cytoplasm
214 (Figure 3B, C). Importantly, internalization of LNP-LR by L-forms could be blocked by the
215 addition of sodium azide (1, 2.5 and 10 mM) or incubation of cells at 4°C, conditions that are
216 commonly used to inhibit endocytosis (Atkinson et al., 2002; Hoffmann and Mendgen, 1998;
217 Sato et al., 2009; Subramanya et al., 2009). Under such conditions, the LNPs only localized to
218 the cell membrane rather than forming foci inside the cell (Figure 3D, E and Figure S3D-E).

These results are consistent with an uptake process of LNPs that is energy-dependent, whereby the particles are internalized by a membrane invagination process.

High-resolution imaging of L-forms using cryo-FIB-SEM

To better understand their ultrastructure and composition, the intracellular vesicles were imaged using 3D cryo-correlative light and electron microscopy (cryo-CLEM) (Figure 4A). Cryo-FIB-SEM (Focused Ion Beam - Scanning Electron Microscopy) allows the 3D high resolution imaging of L-forms and internal vesicles. The cryogenic sample preparation and imaging ensures that the L-forms are visualized in a near-to-native state (Shimoni and Muller, 1998; Studer et al., 1989).

Following high-pressure freezing, cells with putative intracellular vesicles were detected based on internal darker regions lacking cytosolic eGFP using *alpha* pIJ82-GFP (Figure S4). Specific L-forms (example of selection in Figure 4B, C) were imaged in detail using cryo-FIB-SEM. The reduction in cytosolic eGFP indeed matched the presence of internal vesicles as detected by FIB-SEM (Figure 4C, D, white arrow), in line with previous results (Figure 2B). In addition, the composition of the cytoplasm and internal vesicle content was different, as measured using the InLens energy selective backscattered (EsB) detector which provides contrast based on the distribution of heavier elements (Figure 4E). Analysis of the pixel intensity indicated that the contrast level inside the internal vesicle was similar to the extracellular environment, whereas the cytoplasm had a higher contrast. Moreover, an over-exposure experiment showed that the vesicle has the same capacity to absorb the electron dose as the medium outside, different from the rest of the cell (Figure S5A-B). These results support the finding that internal vesicles contain extracellular medium and are formed via membrane invagination (Figure 2C).

Further high-resolution imaging indicated the presence of multiple internal vesicles within individual cells (Figure 4F-I, Figure S5C-E). Most detected vesicles were lining the cell membrane (Figure 4G, Figure S5C-E), varied in size and membrane thickness (Figure 4H) and could even be present inside larger vesicles (Figure 4H and Figure S6D), like the previously observed secondary vesicle (Figure S2F). In addition, vesicles could be observed budding out of the cell membrane (Figure 4I). 3D reconstruction of the budding vesicles based on contour tracing revealed that these were either an extension of an internal vesicle, or remained connected to internal vesicles, forming a complex (Figure 4J-K, Figure S6A-D, Video S2 and S3).

In some cases, cells contained intracellular regions with different grey values from the rest of the cell (Figure 4Li). These regions had a size distribution of 300 to 800 nm, did not line the cell membrane, and were surrounded by dark particles of around 25-60 nm in diameter (Figure 4Lii-iv). It could be possible that these dark particles are lipid bodies, compared to previous cryo-FIB-SEM observations (Spehner et al., 2020; Vidavsky et al., 2016). A potential interpretation is that the internal regions are vesicles of which the enclosing lipid membrane has partially degraded. The lipids and lipidic degradation products may have accumulated in lipid droplets that result in the observed black particles.

These results further confirm that the internal vesicles observed in *K. viridifaciens* L-forms contain external medium and can be formed by invagination of the cell membrane. L-forms can contain multiple vesicles of varying sizes, in some cases forming clusters or complexes of vesicles that can protrude out of the cell membrane. Internal vesicles may release their contents in the cell after vesicle degradation. These findings support a model for uptake of macromolecules such as DNA by engulfment, followed by release of the cargo after vesicle disruption (Figure 5).

DISCUSSION

The bacterial cell wall is an important protective barrier towards the environment, providing stress resistance and enabling the selective passage of molecules. However, in recent years it has become clear that under some conditions, bacteria may also thrive without this layer. Prolonged exposure to environmental stresses, such as cell-wall targeting agents or a high osmotic pressure, can induce the formation of L-forms that efficiently proliferate without their cell wall (Allan et al., 2009; Ramijan et al., 2018). The consequences of such a wall-deficient bacterial lifestyle on their ability to take up DNA are largely unknown. Here we provide evidence that L-forms may take up DNA and other macromolecules via engulfment and the subsequent formation of internal vesicles (Figure 5).

A new mechanism for HGT?

Well-known mechanisms for HGT are natural transformation, transduction, and conjugation (as reviewed in Arnold et al., 2021; Thomas and Nielsen, 2005). These mechanisms require sophisticated machinery to enable transport of DNA across the cell envelope. We here show that wall-deficient cells such as protoplasts, S-cells and L-forms of *K. viridifaciens* take up DNA using PEG. Importantly, L-forms are the only wall-deficient cells that achieve natural transformation using plasmid DNA without PEG. Naturally transformable bacteria use a canonical and complex system for DNA uptake across the cell wall and cell membrane. The latter step requires the DNA-binding protein ComEA and the pore-forming channel protein ComEC, with homologs found across naturally transformable Gram-positive and Gram-negative species (e.g., ComE and ComA in *N. gonorrhoeae*). Disruption of either of these proteins typically results in a drastic reduction or even absence of transformation (Friedrich et al., 2001; Hahn et al., 1987; Inamine and Dubnau, 1995; Yeh et al., 2003). However, disruption of the likely genes for ComEA and ComEC in L-forms of *K. viridifaciens* had no effect on the

293 ability to take up DNA, suggesting a mechanism independent of the canonical DNA
294 translocation machinery.
295
296 **An endocytosis-like process in L-form bacteria**
297 Endocytosis is a fundamental and highly regulated process in eukaryotes that is involved in the
298 uptake of nutrients, regulation of plasma membrane composition, sensing of the extracellular
299 environment and signaling (Thottacherry et al., 2019). Invagination of the membrane and
300 subsequent membrane scission and vesicle formation allows cells to internalize a wide array of
301 cargo such as fluids, ligands, plasma membrane proteins and sometimes even entire bacteria.
302 Invagination is often followed by passing the cargo through the endosomal pathway and
303 lysosomal degradation (Cossart and Helenius, 2014). Specific mammalian cells can take up
304 DNA, followed by active gene expression (Wolff et al., 1990), which potentially occurs via
305 endocytosis, although the exact mechanism is unclear (reviewed by Budker et al., 2000;
306 Trombone et al., 2007; Wolff and Budker, 2005).
307 This work shows that L-forms use an endocytosis-like mechanism for the uptake of
308 DNA, whereby membrane invagination led to the formation of intracellular vesicles that during
309 their formation encapsulated extracellular material (Figure 5). Via this process, not only DNA
310 but also other macromolecules such as 3 kDa dextran and even 125-nm lipid nanoparticles
311 were taken up, strongly suggesting that the uptake process is non-specific. Interestingly, an
312 older study also reports the uptake of fluorescent dextrans in internal vesicles of *Bacillus*
313 *subtilis* L-forms, which was proposed to occur via fluid-phase endocytosis (Oparka et al.,
314 1993).
315 The mechanism underlying formation of intracellular vesicles in L-forms most likely
316 depends on increased membrane dynamics due to excess membrane synthesis (Mercier et al.,
317 2013; Studer et al., 2016). An imbalance in the cell surface to volume ratio due to excess

318 membrane synthesis can lead to internal vesicle formation in spherical *E. coli* and *B. subtilis*
319 shape mutants (Bendezu and de Boer, 2008; Mercier et al., 2013). Internal vesicles or vacuoles
320 can also be formed in enlarged protoplasts and spheroplasts (containing an outer membrane)
321 which are maintained in conditions that allow cell membrane expansion (Nishida, 2020;
322 Takahashi et al., 2020). Indeed, a lack of excess membrane production may also explain why
323 we did not observe consistent DNA uptake in protoplasts and S-cells, both of which are unable
324 to proliferate without their wall.

325 High-resolution electron microscopy imaging revealed multiple internal vesicles inside
326 L-forms. Interestingly, the L-forms also contained regions not surrounded by a membrane but
327 were lined with darker spots that may represent lipid bodies (Spehner et al., 2020; Vidavsky et
328 al., 2016), possibly originating from the degradation products of the membrane of internal
329 vesicles. This disintegration would lead to release of the cargo into the cytoplasm. In
330 eukaryotes, escape of therapeutics from endosomal vesicles can be mediated by bacterial, viral,
331 and chemical agents or by nanoparticles (Patel et al., 2019; Varkouhi et al., 2011). Escape
332 mechanisms include pore formation, destabilization of the membrane, nanoparticle swelling or
333 osmotic rupture. High sucrose levels or the proton sponge effect facilitate the influx of protons
334 followed by chloride ion accumulation and inflow of water, leading to rupture of the vesicle
335 (Behr, 1997; Cervia et al., 2017; Ciftci and Levy, 2001; Liang and W. Lam, 2012).
336 Acidification of endosomes occurs via membrane-localized vacuolar ATPases (V-ATPases)
337 that pump protons into the vesicles (Forgac, 2007). Bacteria have similar proton pumps called
338 F-ATPases on their plasma membrane and have been found on the membrane of intracellular
339 vesicles of enlarged protoplasts (Hensel et al., 1996; Mulkidjanian et al., 2007; Takahashi et
340 al., 2020). Considering the complexity of known escape mechanisms further research is
341 required to understand if and how internal L-form vesicles can disintegrate to release their
342 contents in the cytoplasm.

An endocytosis-like mechanism for macromolecule uptake in primordial cells

L-forms have been proposed as a model to study early lifeforms due to their lack of cell wall and biophysical way of proliferation (Briers et al., 2012b; Errington et al., 2016). Horizontal gene transfer is thought to have played a pivotal role in the evolution of early life (Woese, 1998; Woese, 2000). This may have occurred in cells that did not yet evolve a cell wall, allowing genetic recombination after cell fusion or lightning-triggered electroporation (Errington, 2013; Kotnik, 2013), yet other mechanisms of HGT were unknown. Internal vesicles have also been observed in L-forms of other species, with varying functions and mechanisms of vesicle formation described (Han et al., 2015; Yabu, 1991) . L-forms of *Listeria monocytogenes* are capable of forming DNA-containing internal vesicles along the inside of the cell, which upon release become metabolically active (Briers et al., 2012a; Dell'Era et al., 2009), as well as forming internal vesicles via membrane invagination (Studer et al., 2016). Additionally, secondary invagination of the vesicle membrane itself can result in vesicles containing cytoplasm and represent viable offspring.

These examples provide additional support for the existence of bacterial endocytosis, and we therefore propose that this may reflect an ancient mechanism that has been retained in modern cells to allow shedding their cell wall when the environmental conditions require it.

These examples provide additional support for the existence of bacterial endocytosis, and we therefore propose that this may reflect an ancient mechanism of how primordial cells acquired new genetic material and nutrients via engulfment.

In conclusion, our work shows that the permanent loss of the bacterial cell wall allows the uptake of DNA, dextran and 125 nm-sized lipid nanoparticles via internal vesicle formation. The invagination of the cell membrane, likely driven by excess membrane production, leads to the engulfment of external fluids and subsequent vesicle formation. This is an energy-dependent process that has similarities to a simple form of endocytosis as seen in

368 eukaryotes. Future studies are required to further understand the molecular mechanisms behind
369 this process.
370
371 **ACKNOWLEDGEMENTS**
372 R.K. and L.Z. are supported by the TARGETBIO program of the Netherlands Organization for
373 Scientific Research (NWO), grant nr. 15812. S.S. is supported by the NWA startimpulse grant
374 (Origins Centre). As part of the COFUND project oLife, D.A. acknowledges funding from the
375 European Union's Horizon 2020 research and innovation program under the Grant Agreement
376 847675. M.d.B, R.R., D.D. and A.A. are supported by an ERCAdvanced Investigator grant
377 (H2020-ERC-2017-ADV-788982-COLMIN). A.A. is also supported by the NWO
378 (VI.Veni.192.094). We thank Nico Sommerdijk (Radboudumc, Electron Microscopy Center)
379 for his contribution with high pressure freezing of the samples.
380
381 **AUTHOR CONTRIBUTIONS**
382 R.K. and S.S. carried out the experiments. L.Z., S.S. and R.K. created the plasmids and D.A
383 provided the lipid nanoparticles. A.A., M.d.B, R.R. and D.D. performed the FIB-SEM imaging
384 and analysis. All authors contributed to the design of the experiments and discussion of the
385 results. R.K, D.C. and A.A. wrote the manuscript with input from all authors.
386
387 **DECLARATION OF INTERESTS**
388 The authors declare no competing interests.

FIGURE LEGENDS

Figure 1. Natural DNA Uptake of Wall-Deficient Cells Is Independent of the Competence Proteins ComEA and ComEC and Correlates with Membrane Fluidity

(A) Schematic representation of the different wall-deficient cell types of *K. viridifaciens* that can be created artificially (protoplasts) or naturally (S-cells and L-forms). PG = peptidoglycan.

(B) Mycelium, protoplasts, S-cells and L-form lines *alpha*, M1 and *delta* were incubated with plasmid DNA (pRed*) for 24h, plated on selective medium and incubated at 30°C to select for transformed cells. Note that only L-forms show consistent DNA uptake.

(C) Localization of putative ComEA and ComEC genes (BOQ63_29625 and BOQ63_29630, respectively) on the chromosome of *K. viridifaciens* DSM 40239 as compared to *comEC* and *comEA* of naturally transformable *Bacillus subtilis* str. 168.

(D) Natural transformation assay of 7-day of *alpha* and *alpha*ΔcomEA/EC using pFL-*ssgB*. ns = not significant (n=5 replicates, two-tailed independent t-test, $t(8)=1.572$, $P=0.155$). Data are represented as mean ±SD with individual data points.

(E) Natural transformation efficiency of 1-, 3- and 7-day old *alpha* after 24 h incubation with pFL-*ssgB*. Asterisks indicate statistically significant different transformation efficiency (n=4 replicates, one-way ANOVA, $F(2,9) = 12.16$, Tukey post-hoc test, $P = .006$ (1-3 day) and .005 (1-7 day)). Data are represented as mean ±SD with individual data points.

(F) Generalized polarization as measurement of membrane fluidity of 1-, 3- and 7-day old *alpha* as calculated from the shift in the fluorescence emission spectrum of the membrane dye Laurdan. Lower GP indicates a higher membrane fluidity. Data are represented as mean ±SD with individual data points, n=3.

Figure 2. Formation of Internal Vesicles and Uptake of External Fluids in L-forms

(A) Fluorescence micrograph of *alpha* pIJ82-GFP (cytoplasmic eGFP; green) incubated with Cy-5 labelled plasmid DNA (pFL-*ssgB*; magenta). BF = Brightfield. Scale bar = 2 µm.

(B) Incubation of *alpha* pIJ82-GFP with the membrane-impermeable dye SynapseRed C2M (SynapseRed; magenta), showing two z-slices of one L-form cell. BF = brightfield. Scale bar = 2µm.

(C) Stills of a time-lapse imaging experiment of *alpha* producing DivIVA-eGFP (*alpha* pKR2) (green) incubated with 3 kDa Dextran-Texas Red (D-TR; magenta). Arrows indicate localization of DivIVA-eGFP. Scale bar = 2µm. See also Video S1.

(D) Formation of foci and ring-structures of DivIVA-eGFP in *alpha* pKR2 (green) incubated with Dextran-Texas Red (D-TR, magenta). Scale bar = 2µm. Note that L-forms are able to take up fluorescently stained DNA and Dextran by formation of internal vesicles.

Figure 3. Localization of Lipid Nanoparticles in Internal L-form Vesicles

(A-B) Localization of LNP-LR (Lipid Nanoparticle containing 18:1 Liss Rhod PE; magenta) in internal vesicles of *alpha* (A) and *alpha* pIJ82-GFP (B) after overnight or 3-day incubation at 30°C respectively. Scale bar = 2µm.

(C) Density profile plot and corresponding line selection of *alpha* pIJ82-GFP incubated with LNP-LR showing a decrease in cytoplasmic eGFP emission correlates with an increase in LNP-LR emission.

(D-E) Localization of LNP-LR during incubation with *alpha* at 4°C (D) or in the presence of 2.5 mM sodium azide at 30°C (E) after 0, 24 and 48 h incubation. Similar results were obtained with 1 and 10 mM sodium azide (data not shown). Scale bar = 5 µm. Note that incubation of L-forms with lipid nanoparticles (average size of 125 nm) results in their localization inside internal vesicles, a process that can be inhibited by incubation at 4°C or sodium azide.

Figure 4. 3D Cryo-Fluorescence and Cryo-FIB-SEM of L-forms Reveals its Ultra-Structure in High Resolution

(A) Correlated fluorescence and electron micrographs of the frozen sample (Zen Connect image). The bright green dots indicate individual cells of *alpha* pIJ82-GFP. A finderTOP raster visible both in fluorescence and electron microscopy facilitates alignment between the two imaging modules. The small squares indicate different regions of interest, imaged at higher resolution. FL: Fluorescence light

(B) Higher resolution image of one region of interest, showing many fluorescent cells.

(C) L-form depicted by white box in B, showing intracellular dark sphere (~ 1 micrometer, white arrow).

(D) SEM image (SE, Inlens) of cell in C) with white arrow indicating the internal vesicle. The X, Y and Z arrows in B, C and D indicate the 3D orientation of the imaged cell as observed in 3D FIB-SEM.

(E) Superposition of five consecutive slices (backscattered images) of cell in D). Inset: Intensity plot profile (white) of the region in white box.

(F-I) FIB-SEM slices showing different types of internal vesicles. (F-G) Vesicles lining the cell membrane. Asterisks indicate vesicles. (H) Vesicle complex, note the different membrane thickness of vesicles indicated with white arrows. See also Figure S6D and Video S3. (I) Membrane protrusions as indicated with white arrow.

(J-K) Analysis of the interconnected vesicles of the cell in I). (Ji-iii) Three consecutive slices showing the interaction of different vesicles. Ki-iii show higher magnification of the regions in white boxes in Ji-iii, respectively). (Jiv, Kiv) 3D segmentation of Ki-iii. While some of the vesicles are intracellular, others protrude out of the cell. A complete connected vesicle structure is shown in green and is indicated by white arrows in I, Jiii and Jiv. See also Figure S6A-C and Video S2.

464 (L) Regions with different contrast are lined with black particles representing putative lipid
465 bodies. The size distribution of the black particles is between 25 to 60 nm. Scale bars represent
466 500 nm unless otherwise specified.
467
468 **Figure 5. Proposed Model for DNA Uptake by Internal Vesicle Formation in L-forms**
469 Excess membrane synthesis results in invagination of the cell membrane, leading to the
470 formation of internal vesicles in L-forms. In this process, extracellular liquid containing DNA
471 or other macromolecules is engulfed. Finally, DNA is released from internal vesicles by an
472 unknown process (indicated by dashed arrow), which may involve vesicle disruption. Image
473 created with BioRender.com.
474
475

SUPPLEMENTAL FIGURE LEGENDS

Figure S1. Analysis of Natural and Artificial DNA Uptake and Membrane Fluidity of Cell-Wall Deficient Cells and Confirmation of *alpha*Δ*comEA/EC* Mutant, Related to Figure 1

(A) (Left) Transformation plates showing absence of natural transformation upon incubation of 1-and 7-day old L-form *alpha* with intact or fragmented gDNA of *alpha*Δs*sgB* containing an apramycin resistance cassette. (Right) Gel electrograph of 100 ng intact (I) or fragmented (F) gDNA of *alpha*Δs*sgB* as used in the natural transformation assay.

(B) Polyethylene glycol (PEG)-based transformation efficiency of *K. viridifaciens* mycelium, protoplasts, S-cells and L-forms using plasmid DNA (pRed*) containing an apramycin resistance gene, shown as the percentage of transformed colonies per total colony forming units. Data are represented as mean ± SD, n=3.

(C) PEG-based transformation of *alpha* using unmethylated or methylated plasmid DNA (pRed*), gDNA or filter-sterilized salt-lysed cells from mutant line *alpha*Δ*ssgB*.

(D) Gel electrograph of PCR products from three different PCR mixes to confirm the replacement of *comEA* and *comEC* by an apramycin resistance cassette. WT = gDNA *alpha*; Δ = gDNA *alpha*Δ*comEA/EC*. Expected products: PCR 1 WT = 3676 bp, mutant = 1294 bp; PCR 2 WT = 1197 bp, mutant = no amplification, PCR 3 WT = 745 bp, mutant = no amplification.

(E) Generalized Polarization (GP) as measure of membrane fluidity of *K. viridifaciens* protoplasts, 1-, 3- and 7- day old L-form *alpha*. Lower GP indicates higher fluidity. *, ** and *** indicate $P \leq 0.05$, 0.01 and 0.001, respectively (one-way ANOVA, $F(3,8) = 19.49$, Tukey post-hoc test, n=3). Data are represented as mean ±SD with individual data points, n=3.

(F) Membrane fluidity of L-form *alpha* (1- and 7-day old), S-cells and protoplasts of *K. viridifaciens*. Top rows show brightfield images and heatmap of fluorescence emission (red to

blue colour indicate GP values of -1.0 to 1.0 respectively) of representative cells stained with a Laurdan dye for quantifying the membrane fluidity (BF = brightfield, FL = fluorescence emission). Bottom panel shows frequency distributions of the Generalized Polarization (GP). Lower GP values correspond to higher membrane fluidity indicating that L-forms have more fluid membranes compared to S-cells and protoplasts. Control = cells imaged and analysed without Laurdan staining.

Figure S2. Analysis of DNA Content, Internal Vesicles and Uptake of D-TR of Cell-Wall Deficient Cells, and effect of *divIVA* deletion on DNA Uptake, Related to Figure 2

(A) *alpha* pIJ82-GFP incubated without Cy-5 DNA as fluorescence control.

(B) *alpha* and *alpha* pRed* stained with SYTO-9 (green) to indicate chromosomal DNA. *alpha* is stained with SynapseRed C2M (SynapseRed; magenta) to visualize cell membranes, whereas (absence of) cytosolic mCherry for *alpha* pRed* (magenta) indicates the presence of an internal vesicle.

(C) Protoplasts and S-cells of *K. viridifaciens* pIJ82-GFP producing cytosolic eGFP incubated with SynapseRed for 72 h (top rows), and S-cells of *K. viridifaciens* pRed* producing cytosolic mCherry incubated with SynapseRed (SR) and SYTO-9 for 72 h (bottom row). Chromosomal DNA is visualized using SYTO-9 staining. Note that presence of internal membrane structures causes a reduction in cytosolic fluorescence emission.

(D) Natural transformation assay of 7-day old *alpha* and *alpha*Δ*divIVA* using pFL-*ssgB*. ns = not significant (two-tailed independent t-test, $t(8)=0.489$, $P=0.638$). Data are represented as mean ± SD with individual data points, n=5.

(E) L-forms without DivIVA can produce internal vesicles as shown for 5-day old *alpha*Δ*divIVA* pIJ82-GFP producing cytosolic eGFP. Scale bar = 2 μm.

(F) *alpha* incubated with (example 1 and 2) or without (control) Dextran Texas-Red (D-TR; magenta), showing the formation of internal vesicles filled with D-TR. The arrow indicates the presence of a non-fluorescent secondary internal vesicle inside an existing internal vesicle (example 2). Scale bar = 5 µm.

(G) Protoplasts and S-cells of *K. viridifaciens* pIJ82-GFP incubated with D-TR for 72 h. Note that no internalization of D-TR was observed.

Figure S3. Uptake of LNP-LR by *alpha*, Related to Figure 3

(A) *alpha* pIJ82-GFP incubated without LNP-LR (LNP-Liss Rhod; magenta) as imaging control.

(B-C) *alpha* incubated with (B) or without (C) LNP-LR showing localization of LNP-LR after 0 h, 24 h and 48 h or examples of autofluorescence, respectively.

(D-E) *alpha* incubated with PBS at 4 degrees (D) or with PBS at 30°C in the presence of 2.5 mM sodium azide (E) as control for fluorescence emission. Images were obtained after 0, 24 and 48 h incubation.

Figure S4. High Resolution Cryo-Fluorescence of L-forms, Related to Figure 4

alpha pIJ82-GFP imaged using cryo-fluorescence microscopy. Putative vesicles are indicated with arrows. Images were captured using the long distance 100x objective.

Figure S5. Over-dose experiment of L-form Cell using FIB-SEM, Related to Figure 4

(A-B) FIB-SEM slice of over-dose experiment using *alpha* pIJ82-GFP. The yellow colour in B) indicates areas with distinguished beam damage. The vesicle (black asterisk in the center of the cell) seems to be less to none affected by the dose, similar to the medium outside the cell (black asterisk outside of the cell). The image in Figure 4D is taken before this experiment,

and Figure 4E is obtained by summing several slices deeper in the cell after acquiring this image.

(C-E) FIB-SEM slices of two cells (C-D correspond to the cell in Figure 4F and E corresponds to the cell in Figure 4 H-K), white arrows indicate vesicles that line the cell membrane. Scale bar in C-E is 0.5 µm.

Figure S6. 3D Segmentation of L-form Vesicles, Related to Figure 4

(A-C) FIB-SEM slices corresponding to Figure 4I, Jiv and Ki-iii, respectively. Colours correspond to the segmented colours in Figure 4Kiv. Vesicles that are budding out the cells are connected to other vesicles or are elongated inside the cell. Scale bar = 200 nm. See also Video S2.

(D) FIB-SEM slices corresponding to the cell in Figure 4H. Z-number indicates the slice. Colours indicate individual vesicles. See also Video S3.

MATERIALS AND METHODS

Bacterial strains and culture conditions

The bacterial strains and plasmids used in this study are listed in Table S2 and S3 respectively. *Kitasatospora viridifaciens* DSM40239 (Ramijan et al., 2017) was grown confluently on maltose-yeast extract medium (MYM) to obtain spores, which were harvested after 3-4 days of growth (Stuttard, 1982). For mycelial growth in liquid, strains were grown at a density of 1 x 10^6 spores ml^{-1} for two days in LPB medium without sucrose at 100 rpm, while LPB with sucrose was used to induce the formation of S-cells (Ramijan et al., 2018). L-forms were grown on solid L-phase medium agar (LPMA) or liquid LPB medium (Ramijan et al., 2018). Liquid cultures were inoculated with spores for *K. viridifaciens* strains or with a frozen aliquot of a 1-2-day old L-form culture in case of L-form strains. L-forms were grown in liquid culture for 3-4 days for chemical transformation and 7 days for all other experiments unless stated specifically. L-forms were adjusted to 5-7.5 x 10^7 CFU ml^{-1} for transformation assays (based on OD_{600} of 3 for 3- and 7-day old cells and 0.2 for 1-day old cells), and 2.5-5 x 10^7 CFU ml^{-1} (OD_{600} of 2) for all other experiments with 7-day old cells. All *Kitasatospora* cultures were grown at 30°C.

Escherichia coli strains were grown on solid or liquid LB medium (while shaking at 250 rpm) at 37°C. Where necessary, antibiotics (100 µg ml^{-1} ampicillin, 25 µg ml^{-1} chloramphenicol, 5 µg ml^{-1} thiostrepton, 50 µg ml^{-1} apramycin, 100 µg ml^{-1} hygromycin B with the exception of 200 µg ml^{-1} hygromycin B for LB medium) were added to the culture medium. *E. coli* JM109 (Yanisch-Perron et al., 1985) was used for cloning purposes, while *E. coli* ET12567/pUZ8002 (MacNeil et al., 1992) was used to obtain methylation-deficient DNA.

587 **Construction of plasmids**

588 All PCRs were performed using PFU or Q5® High-Fidelity DNA polymerase (NEB). The
589 primers used in this study are listed in Table S4. To create pFL-*ssgB* (Table S3), a hygromycin
590 resistance cassette was amplified using primer pair Hyg_F-231_EEV and Hyg_R+1237_HEV
591 with pMS82 (Gregory et al., 2003) as the template. The PCR products were digested with
592 EcoRV and cloned into pWHM3-oriT (Wu et al., 2019) to generate pWHM3-oriT-hyg (Table
593 S3). The 3' flank of *ssgB* was digested from pKR1 (Ramijan et al., 2018) and cloned into
594 pWHM3-oriT-hyg using XbaI and HindIII to generate the final plasmid.

595 pRK1 (Table S3) was created by amplifying the upstream flanking region of *comEA* by
596 PCR with primers FL1-comEA/comEC-FW and FL1-comEA/comEC-REV, thereby
597 introducing unique EcoRI and XbaI resitricion sites, while the downstream flanking region of
598 *comEC*, made by gene synthesis (Baseclear, Leiden, the Netherlands) was flanked by XbaI and
599 HindIII sites. The flanking regions and apramycin cassette were cloned in pWHM3-oriT using
600 the EcoRI, HindIII restriction sites interspersed with an apramycin resistance cassette
601 containing flanking XbaI sites, thereby creating the final plasmid. The *comEA/comEC* deletion
602 mutant was created in L-form strain *alpha* (Ramijan et al., 2018) using pRK1, which replaced
603 the nucleotides +58 relative to the startcodon of *comEA* (BOQ63_29625) until + 2489 relative
604 to the startcodon of *comEC* (BOQ63_29630) with an apramycin resistance cassette. Note that
605 the gene annotation of *Streptomyces viridifaciens* ATTC11989 (accession CP023698) was
606 used to determine the putative correct start and stop codons for *comEC*.

607 To create pIJ82-GFP, the region containing the *eGFP* gene with a *gap1* promoter was
608 amplified from plasmid pGreen (Zacchetti et al., 2016) using primer pair gap1_FW_BglII and
609 egfp_RV_EcoRI. The resulting PCR product was cloned into pIJ82 using BglII and EcoRI to
610 generate the final plasmid.

611

612 **Construction of bacterial strains**

613 To create new strains, transformation of L-form *alpha* with plasmid DNA was achieved using
614 chemical transformation based on polyethylene glycol (PEG) (Kieser et al., 2000). Plasmid
615 DNA was isolated from *Escherichia coli* ET12567/pUZ8002 to obtain methylation-deficient
616 DNA. L-form strains *alpha* pIJ82-GFP and *alpha*Δ*divIVA* pIJ82-GFP were created using
617 chemical transformation of *alpha* and *alpha*Δ*divIVA* with pIJ82-GFP respectively, followed
618 by selection with hygromycin B (Table S2). The strains were verified using the detection of
619 fluorescent eGFP production using fluorescence microscopy. Strain *alpha*Δ*comEA/EC* was
620 obtained by chemical transformation of *alpha* with pRK1 followed by selection for apramycin
621 (Table S2). Subsequent growth on non-selective medium allowed for double homologous
622 recombination leading to replacement of the *comEA/EC* region by an apramycin resistance
623 cassette, leading to thiostrepton-sensitive, apramycin-resistant cells. The strain was verified by
624 PCR using primer pair ComEA_Apra_check_FW and ComEC_Apra_check_RV to confirm
625 replacement of the region by the apramycin cassette. To further confirm deletion of this region,
626 PCR was performed using primer pairs ComEC_Presence_Check_1_FW/RV and
627 ComEC_Presence_Check_2_FW/RV, which amplify parts of *comEC* only if this genomic
628 region is still present.
629
630 **Genomic DNA preparation**
631 Genomic DNA was isolated from a 5-day old culture of *alpha*Δ*ssgB* (Ramijan et al., 2018)
632 using phenol:chloroform extraction (Kieser et al., 2000). Briefly, the cell pellet was
633 resuspended in 10.3% sucrose containing 0.01M ethylenediamine tetraacetic acid (EDTA)
634 pH8 following lysis with 10% sodium dodecyl sulfate (SDS). Extraction with
635 phenol:chloroform was performed and the nucleic acids were precipitated using isopropanol.
636 The pellet was dissolved in Tris-EDTA buffer followed by RNase A (Thermo Fisher) and

637 Proteinase K treatment (Qiagen). The gDNA was isolated using phenol:chloroform extraction
638 and precipitated using absolute ethanol, before resuspension in nuclease-free water.
639 Fragmented gDNA was obtained by beat-beating the intact gDNA for 12 minutes using 2 mm
640 diameter glass beads in a Mikro-Dismembrator U (Sartorius) at 2000 rpm. Chromosomal DNA
641 concentrations were verified using the Quant-IT™ Broad-Range dsDNA Assay Kit
642 (Invitrogen).
643
644 **Preparation of protoplasts from *Kitasatospora***
645 *K. viridifaciens* strain DSM40239 was inoculated at a density of 5 x 10^6 spores ml^{-1} in
646 TSBS:YEME (1:1) liquid medium with 0.5% (w/v) glycine and 5 mM $MgCl_2$. The culture was
647 grown for 48 h while shaking at 200 rpm, after which protoplasts were prepared as described
648 (Kieser et al., 2000). Cultures of 72 h were used for *K. viridifaciens* pIJ82-GFP and pRed*.
649 Lysozyme treatment was performed by the addition of 10 mg ml^{-1} of chicken egg-white
650 lysozyme (Sigma 70 000 U mg^{-1}) to the mycelial suspension. The cells were incubated for 2-3
651 h at 100 rpm and 30°C, after which mycelial fragments were separated from the protoplasts by
652 filtration trough a cotton wool filter (Kieser et al., 2000).
653
654 **Isolation of S-cells from *Kitasatospora***
655 S-cells were isolated from LPB cultures by filtration (Ramijan et al., 2018). In short, the culture
656 was filtered through a sterile EcoCloth™ filter (Contec) and subsequently passed through a 5
657 µm Isopore™ membrane filter. The cells were concentrated by gentle centrifugation at 1000
658 xg for 20 minutes, after which 90% of the supernatant was removed. The cell pellet was
659 suspended carefully in the remaining liquid.
660
661

662 **Chemical transformation**

663 Polyethylene-glycol (PEG) was used for transformation as described (Kieser et al., 2000),
664 using freshly prepared protoplasts, S-cells or L-forms that were kept on ice prior to
665 transformation. For chemical transformation, 50 µl of cells were mixed with 1 µg pRed*
666 (Zacchetti et al., 2018), 150 ng gDNA of strain *alpha*Δ*ssgB*, filter-sterilized salt-lysed cells (35
667 ng DNA from *alpha*Δ*ssgB*) or MilliQ. Then, 200 µl of 25% (w/v) PEG1000 in P-buffer (Kieser
668 et al., 2000) was added to the cells, followed by gently mixing and diluting the suspension in
669 P-buffer. Serial dilutions were plated on LPMA medium and after 16-18 h incubation an
670 overlay was performed with 1 ml of P-buffer containing antibiotics. Colony forming units
671 (CFU) were counted after 7 and 14 days for L-forms and S-cells/protoplasts, respectively.
672 Transformants were verified by streaking on selective medium and microscopy.
673
674 **Natural transformation assay**
675 Freshly prepared cells were incubated with 30 ng μl^{-1} DNA or MilliQ for 18-24 h at 100 rpm.
676 A final concentration of 100 and 10 ng μl^{-1} intact gDNA and 10 ng ul^{-1} for fragmented gDNA
677 isolated from *alpha*Δ*ssgB* was used in combination with both 1- and 7-day old *alpha*. Dilutions
678 were plated on selective and nonselective LPMA after careful resuspension. Colony forming
679 units were determined after 7-day incubation at 30°C for L-forms and mycelium and up to 14
680 days for protoplasts and S-cells. Transformants were verified by growth on selective medium
681 and by PCR (using primers Tsr_Hyg_FW1 and Tsr_Hyg_RV1) or microscopy. Cells were
682 prepared from at least five replica cultures to compare transformation efficiencies between
683 strains.
684
685

686 **Membrane fluidity**

687 Three replicate cultures of 1, 3 and 7-day old L-forms or freshly prepared protoplasts were
688 subjected to a Laurdan dye assay as a measure for membrane fluidity (Scheinpflug et al., 2017).
689 1 ml of each culture was first centrifuged at 1000 xg for 10 minutes to remove any traces of
690 the culture media. Cells were resuspended in 1 ml P-buffer and adjusted to an OD_{600} of 0.6. 10
691 mM Laurdan (6-Dodecanoyl-2-Dimethylaminonapthalene) stock solution (Invitrogen) was
692 prepared in 100% dimethylformamide (DMF) and stored at -20°C in an amber tube. To each 1
693 ml OD-adjusted culture, 1 µl of Laurdan dye was added to a final concentration of 10 µM. The
694 cultures were then incubated in the dark at 30°C for 10 min, while shaking at 100 rpm. The
695 cells were washed three times with P-buffer containing 1% dimethyl sulfoxide to remove
696 unbound dye molecules before the cells were resuspended in P-buffer. 200 µl of this
697 resuspended culture was aliquoted into a 96-well black/clear glass bottom sensoplate (Greiner
698 Bio-one VWR). Four technical replicas were measured per culture, as well as one replica per
699 culture condition without dye to measure background fluorescence.
700 Sample excitation was performed at 350 nm followed by fluorescence emission capture at 435
701 and 490 nm, determined using a Spark® multimode microplate reader (Tecan). After
702 subtracting the background fluorescence, the generalized polarization (GP) value was
703 calculated using -

$$GP = \frac{I_{435} - I_{490}}{I_{435} + I_{490}}$$

704

705 Values obtained after calculation lie in the range of -1 to +1 with those closer to -1 indicating
706 greater fluidity**.**

707 Preparation of cells for quantification of membrane fluidity by microscopy was
708 performed as following. Cells were washed and OD-adjusted as mentioned above. Laurdan dye
709 (stock concentration 10 mM) was added to 100 µl of culture to get a final concentration of 100

710 µM. The culture was placed in 30°C for 5 min, while shaking at 100 rpm in the dark. 900 µl of
711 prewarmed P-buffer containing 1% dimethyl sulfoxide was added and the culture was
712 centrifuged (1000 xg, 10 min) to remove any unbound dye molecules. The cells were finally
713 resuspended in 100 µl of P-buffer for microscopy analysis. Cells treated similarly but without
714 Laurdan dye were used a control for microscopy measurements.
715
716 **Preparation of fluorescently labelled DNA**
717 Fluorescently labelled plasmid DNA was prepared using The Mirus Label IT® Cy™5 Labelling
718 Kit according to the manufacturer's specifications. Aliquots of labelled DNA (100 ng μl^{-1})
719 were stored at -20°C until further use.
720
721 **Self-assembly of lipid nanoparticles**
722 All lipids (DLin-MC3-DMA/Cholesterol/DSPC/DMG-PEG2k/18:1 Liss Rhod PE) were
723 combined in a molar ratio of 50/38.3/10/1.5/0.2 using stock solutions (100 µM – 10 mM) in
724 chloroform:methanol (1:1). Organic solvents were evaporated under a nitrogen stream and
725 remaining solvent was removed *in vacuo* for at least 1 h. Subsequently, the lipid film was
726 dissolved in $EtOH_{abs}$ and a 50 mM citrate buffer (pH = 4, MilliQ) was prepared. Each solution
727 was loaded into separate syringes and connected to a T-junction microfluidic mixer. The
728 solutions were mixed in a 3:1 flow ratio of citrate buffer against lipids (1.5 mL min^{-1} for citrate
729 buffer, 0.5 mL min^{-1} for lipid solutions) giving a total lipid concentration of 1 mM. After
730 mixing, the solution was directly loaded in a 10k MWCO dialysis cassette (Slide-A-Lyzer™,
731 Thermo Scientific) and dialyzed against 1x Phosphate Buffered Saline (PBS, 137 mM NaCl,
732 2.7 mM KCl, 8 mM Na_2HPO_4 and 2 mM KH_2PO_4) overnight. All incubations with LNPs were
733 performed with cells resuspended in LPB of which the final volume of LNP solution was 25%.
734

735 **Hydrodynamic diameter and zeta-potential measurement**

736 Dynamic light scattering (DLS) measurements were performed on a Zetasizer Nano Series
737 (Malvern Instruments, Malvern, UK). The incorporated HeNe laser works at a wavelength of
738 633 nm and uses a detector at an angle of 173° (noninvasive back scatter technology).
739 Measurements were recorded with 1 min equilibration time in UV cuvettes at 25 °C. For the
740 estimation of z-average diameter (intensity weight mean diameter) and polydispersity index
741 (PDI)(relative width of particle size distribution) samples were prepared by tenfold dilution
742 with 1x PBS. For the estimation of the zeta potential the sample was diluted with 0.1x
743 Phosphate Buffered Saline (13.7 mM NaCl, 0.27 mM KCl, 0.8 mM Na_2HPO_4, and 0.2 mM
744 KH_2PO_4). All the data were in triplicates to obtain the mean value.
745
746 **Fluorescence and light microscopy**
747 Detection of fluorescence emission of transformants was performed using a Zeiss Axioscope
748 A.1 equipped with a Zeiss Axiocam 305 color digital camera, using filter set 63 HE (Carl Zeiss,
749 consisting of a 572/25 nm bandpass excitation filter, 590 nm beamsplitter and 629/62 nm
750 bandpass emission filter) to capture mCherry fluorescence. All other microscopy was
751 performed using a Zeiss LSM 900 confocal microscope with Airyscan 2 module, temperature
752 control chamber and Zen 3.1 software (blue edition, Carl Zeiss Microscopy GmbH). All
753 excitation and emission settings for this microscope are listed in Table S5. Multichannel (DIC
754 and fluorescence) and multistack images were obtained unless specified otherwise. 10 µl of
755 cells were imaged on an 8-chamber slide (ibidi®) coated with 0.1% poly-L-lysine (excess poly-
756 L-lysine was removed and the slide was allowed to dry prior to applying the sample). For
757 timelapse imaging or overnight incubation in the temperature control chamber, 400 µl of cell
758 culture added to a 35 mm imaging µ-Dish (ibidi®) and allowed to settle at 30°C for an hour

759 before overnight imaging. Image analysis was performed using Fiji (ImageJ) software
760 (Schindelin et al., 2012).

761 Chromosomal DNA was visualized after incubation for 30 min with SYTO-9 at a final
762 concentration of 2 µM. Cell membranes were visualized by incubation with SynapseRed C2M
763 (SynapseRed) (PromoKine, PromoCell GmbH) at a final concentration of 0.2 µg ml^{-1}. After
764 overnight incubation in a µ-Dish (ibidi®) using the Zeiss LSM 900 confocal temperature
765 control chamber, cells were imaged using the Airyscan mode with super resolution post-image
766 processing via the Zen software. Protoplasts and S-cells were incubated with SynapseRed up
767 to 72 h before imaging on a glass slide.

768 Uptake of fluorescently labelled DNA was assessed by incubating cells with Cy-5
769 labelled plasmid DNA (pFL-*ssgB*) at a final concentration of 1.25 µg ml^{-1} and was imaged after
770 48 h.

771 To capture internal vesicle formation and uptake of Dextran-Texas Red (D-TR), cells
772 of *alpha* pKR2 were incubated with a final concentration of 1 mg ml^{-1} Dextran-Texas Red
773 (3000 MW, neutral, Molecular Probes) in PBS and were imaged overnight. Multistack imaging
774 across 6 µm total distance with 1.5 µm steps was done with an image captured every 10
775 minutes. Uptake of D-TR in *alpha*, protoplasts or S-cells was assessed after incubation up to
776 72 h.

777 Uptake of red fluorescent LNPs (LNP-LR) by *alpha* was visualized by imaging after
778 overnight incubation in a µ-Dish (ibidi®) or after incubation for up to three days prior to
779 imaging as indicated. Inhibition of LNP uptake was performed by incubation in the presence
780 of 1-, 2.5- or 10-mM sodium azide (Sigma) or incubation at 4°C, and images were obtained
781 using via the Zen software after 0, 24 and 48 h. To determine the subcellular localization of
782 LNP-LR in *alpha* pIJ82-GFP, imaging was performed using the Airyscan mode with super

783 resolution post-image processing and analyzed using the pixel intensity of the red (LNP-LR)
784 and green (eGFP) channels using the Plot Profile tool in Fiji (ImageJ).

785 To measure the membrane fluidity, samples were excited using a 405 nm laser and
786 images were captured at emissions of 430 nm and 500 nm. GP value was calculated using the
787 'Calculate GP' plug-in in Fiji (Vischer, 2016) to obtain a histogram of pixel counts over the
788 range of -1 to +1. Briefly, the image is split into individual channels followed by background
789 subtraction and setting the non-significant pixels to zero. The images are then assigned letters
790 "A" and "B" to calculate A-B and A+B using the image calculator. Finally, a ratio of (A-
791 B)/(A+B) is shown as an image where minimum pixel values are set to -1 (red) and maximum
792 pixel values set to +1 (blue). Using the analyze histogram function a list of values is obtained
793 and used for plotting the distributions of different samples.
794

795 **Cryo-correlative fluorescence and electron microscopy**

796 *High pressure freezing*

797 7-day old L-form stain *alpha* pIJ82-GFP expressing cytoplasmic eGFP was adjusted to OD_{600}
798 of 2 in fresh medium containing 25% (v/v) PBS and a final concentration of 17% sucrose. Cells
799 were incubated for four days, during which cells settled to the bottom. A few microliters of the
800 resuspended L-form pellet was sandwiched between HPF (High-Pressure-Freezing) carriers
801 with 2 mm internal diameter (either 0.1 mm or 0.05 mm cavity, Art. 241 and Art. 390
802 respectively, Wohlwend) and tailor-made grid labeled, flat-sided finderTOP (Alu-platelet
803 labelled, 0.3 mm, Art.1644 Wohlwend) to allow an imprint of a finder matrix on the amorphous
804 ice (de Beer et al., 2021). The finderTOP was treated with 1% L-α-phosphatidylcholine (61755,
805 Sigma) in ethanol (1.00983.1000, Supelco) before freezing. The samples were then high
806 pressure frozen (Live µ, CryoCapCell) and stored in liquid nitrogen until imaging.

To improve correlation between cryo-light and cryo electron microscopy, the frozen samples were loaded into a universal cryo-holder (Art. 349559-8100-020, Zeiss cryo accessory kit) using the ZEISS Correlative Cryo Workflow solution, fit into the PrepDek® (PP3010Z, Quorum technologies, Laughton, UK). Here, the HPF carriers fits into a universal cryo-holder, which subsequently can be placed into an adaptor specific for cryo-light or cryo-electron microscopy.

Cryo-fluorescence imaging to detect regions of interests (ROI)

The frozen samples were imaged with a cryo-stage adaptor (CMS-196, Linkam scientific inc.) applied to an upright confocal microscope (LSM900, Zeiss microscopy GmbH) equipped with an Airyscan 2 detector. Overview images (Zeiss C Epiplan-Apochromat 5x/0.2 DIC) were made with reflection microscopy to visualize the gridded pattern on the ice surface. Next, medium-resolution Z-stack images (Zeiss C Epiplan-Apochromat 10x/0.4 DIC) were taken with a 488 nm laser (0.4%) with a voxel size of 0.15 µm x 0.15 µm x 1.18 µm. Using this resolution, cells of interest could be selected and Z-stack images were created (Zeiss C Epiplan-Neofluar 100x/0.75 DIC) using a 488 nm laser (4%), with a voxel size of 0.08 µm x 0.08 µm x 0.44 µm. In addition, the ice surface was imaged in all ROIs with reflection microscopy for correlation purposes in the FIB-SEM.

Prior to cryo-light imaging, a Zeiss ZEN Connect project (Zeiss software for correlative microscopy, version 3.1) was created to make a working sheet (canvas) to align and overlay all the images and to facilitate further correlation with cryo-FIB-SEM.

3D Cryo-FIB-SEM

The sample was sputter-coated with platinum, 5mA current for 30 seconds, using the prep stage sputter coater (PP3010, Quorum technologies, Laughton, England) and was transferred into the

Zeiss Crossbeam 550 FIB-SEM (Carl Zeiss Microscopy GmbH, Oberkochen, Germany) using the PP3010T preparation chamber (Quorum, Laughton, England). Throughout imaging, the samples were kept at -140 °C and the system vacuum pressure was 1 x 10^{-6} mbar.

After inserting the sample into the FIB-SEM chamber, overview images were taken using the SEM to align the data with the LSM reflection image of the surface of the same ZEN Connect project. This alignment enables the stage registration which allows using the fluorescence signal to navigate to different regions of interest. After initial alignment using the SEM, a FIB image of the surface was collected with the 30kV@10pA probe in 54° tilt.

A coarse trench was milled for SEM observation using the 30 kV@30 nA FIB probe. Cold deposition was done with platinum for 30 sec. Fine FIB milling on the cross section was done using the 30kV@700pA probe. For serial FIB milling and SEM imaging the slice (trench) width was 40 µm and for FIB milling the 30 kV@300pA probe was used, with a slice thickness of 20 nm. When a new slice surface was exposed by FIB milling, an InLens secondary and EsB images were simultaneously collected at 2.33 kV acceleration potential with 250pA probe current. The EsB grid was set to -928 V. The image size was set to 2048 × 1536 pixels. For noise reduction line average with a line average count N = 46 at scan speed 1 was used. The voxel size of all stacks was 5×5×20 nm^3.

3D FIB-SEM Image post processing

The cryo-FIB-SEM images were processed using MATLAB (R2018b, Natick, Massachusetts: The MathWorks Inc.) to correct for defects such as curtaining, misalignment and local charging. The same software was used for subsequent noise reduction and contrast enhancement. A summary of each processing step is as follows:

Curtaining: Removing the vertical stripes in the stacks was done following a wavelet-FFT filtering approach described by (Munch et al., 2009). In brief, the high frequency information corresponding to the vertical stripes was successively condensed into a single coefficient map using decomposition by "coif" wavelet family. Subsequently, a 2D-fourier transform was performed to further tighten the stripe information into narrow bands. Finally, the condensed stipe information was eliminated by multiplication with a gaussian damping function and the destriped image was reconstructed by inverse wavelet transform.

Alignment: The consecutive slices were aligned using normalized cross correlation. Briefly, the first image in the stack was chosen as reference and the second image was translated pixel by pixel across the reference and a normalized cross correlation matrix was obtained using the "normxcorr2" function. The location of the highest peak in the cross-correlation matrix (representing the best correlation) was then used to calculate the translation required to align the two images. Once the moving image was aligned with the reference image, it served as the reference for alignment of the subsequent slice.

Charging: Elimination of the local charge imbalance was achieved using anisotropic gaussian background subtraction. Briefly, the "imgaussfilt" function was used to perform 2D-gaussian smoothing with a two-element standard deviation vector. The elements in the vector were chosen in a manner to apply a broad and sharp gaussian in the horizontal and vertical directions, respectively. Subsequently, the corrected image was obtained by subtracting the filtered image from the original image.

Noise Reduction: In order to improve the signal-to-noise ratio, noise reduction was performed using anisotropic diffusion filtering (Perona and Malik, 1990). Briefly, using the "imdiffuseest" function, the optimal gradient threshold and number of iterations required to filter each image was estimated. Subsequently, the "imdiffusefilt" function was applied with the estimated optimal parameter values to denoise each image.

Contrast enhancement: As the final processing step, the contrast was enhanced using "Contrast-limited adaptive histogram equalization" (Zuiderveld, 1994). Using the "adapthisteq" function, the contrast was enhanced in two steps, using a uniform distribution and a low clipping limit in order to avoid over-amplification of homogeneous regions.

3D segmentation: DragonflyTM image analysis and deep-learning software (version 2021.1, Objects Research Systems, Montreal, QC, Canada) was used to segment all image data.

Bioinformatic search for putative competence genes

Protein sequences from *Bacillus subtilis* str. 168, *Neisseria gonorrhoeae* and *Helicobacter pylori* strain P12 were obtained from the UniProt database or literature (Wolfgang et al., 1999). These sequences were used for a BlastP search against the non-redundant protein sequence database of *Streptomyces viridifaciens* (taxid 48665). Hits belonging to *Streptomyces viridifaciens* strain DSM40239, sequence accession numbers CP090840 to CP090842 with an E-value of $1x10^{-6}$ or lower were collected (Table S1).

Statistics

All statistics were performed using SPSS statistics software (IBM, version 27.0). P-values less than 0.05 were considered statistically significant.

SUPPLEMENTAL VIDEO LEGENDS

Video S1. Uptake of Dextran-Texas Red by L-forms, Related to Figure 2

Timelapse video of *alpha*-DivIVA-eGFP (green) incubated with 3 kDa Dextran-Texas Red (D-TR; magenta). Left: Brightfield. Right: Composite of green and magenta channels. Scale bar indicates 1 µm.

Video S2. 3D Reconstruction of Vesicles in L-form Cell, Related to Figure 4

3D segmentation of *alpha* pIJ82-GFP corresponding to Figure 4 Jiv and Kiv. Colours indicate individual vesicles or vesicle complexes. The cell is depicted in grey.

Video S3. 3D Reconstruction of Vesicles in L-form Cell, Related to Figure 4

3D segmentation of *alpha* pIJ82-GFP corresponding to Figure 4H and Figure S6D. Colours indicate individual vesicles or vesicle complexes. The cell is depicted in grey.

914 **REFERENCES**
915
916 Allan, E.J., Hoischen, C., and Gumpert, J. (2009). Bacterial L-forms. Adv Appl Microbiol *68*,
917 1-39.
918 Araki, N., Johnson, M.T., and Swanson, J.A. (1996). A role for phosphoinositide 3-kinase in
919 the completion of macropinocytosis and phagocytosis by macrophages. Journal of Cell Biology
920 *135*, 1249-1260.
921 Arnold, B.J., Huang, I.T., and Hanage, W.P. (2021). Horizontal gene transfer and adaptive
922 evolution in bacteria. Nat Rev Microbiol.
923 Atkinson, H.A., Daniels, A., and Read, N.D. (2002). Live-cell imaging of endocytosis during
924 conidial germination in the rice blast fungus, Magnaporthe grisea. Fungal Genetics and Biology
925 *37*, 233-244.
926 Behr, J.-P. (1997). The proton sponge: a trick to enter cells the viruses did not exploit. CHIMIA
927 International Journal for Chemistry *51*, 34-36.
928 Bendezu, F.O., and de Boer, P.A. (2008). Conditional lethality, division defects, membrane
929 involution, and endocytosis in mre and mrd shape mutants of Escherichia coli. J Bacteriol *190*,
930 1792-1811.
931 Bierman, M., Logan, R., O'Brien, K., Seno, E.T., Rao, R.N., and Schoner, B.E. (1992). Plasmid
932 cloning vectors for the conjugal transfer of DNA from *Escherichia coli* to *Streptomyces* spp.
933 Gene *116*, 43-49.
934 Briers, Y., Staubli, T., Schmid, M.C., Wagner, M., Schuppler, M., and Loessner, M.J. (2012a).
935 Intracellular vesicles as reproduction elements in cell wall-deficient L-form bacteria. PLoS One
936 *7*, e38514.
937 Briers, Y., Walde, P., Schuppler, M., and Loessner, M.J. (2012b). How did bacterial ancestors
938 reproduce? Lessons from L-form cells and giant lipid vesicles: multiplication similarities
939 between lipid vesicles and L-form bacteria. Bioessays *34*, 1078-1084.
940 Budker, V., Budker, T., Zhang, G., Subbotin, V., Loomis, A., and Wolff, J.A. (2000).
941 Hypothesis: naked plasmid DNA is taken up by cells in vivo by a receptor-mediated process.
942 The journal of gene medicine *2*, 76-88.
943 Cervia, L.D., Chang, C.C., Wang, L., and Yuan, F. (2017). Distinct effects of endosomal escape
944 and inhibition of endosomal trafficking on gene delivery via electrotransfection. PLoS One *12*,
945 e0171699.
946 Chapman, D. (1975). Phase transitions and fluidity characteristics of lipids and cell
947 membranes. Quarterly reviews of biophysics *8*, 185-235.
948 Chen, I., and Dubnau, D. (2004). DNA uptake during bacterial transformation. Nat Rev
949 Microbiol *2*, 241-249.
950 Ciftci, K., and Levy, R.J. (2001). Enhanced plasmid DNA transfection with lysosomotropic
951 agents in cultured fibroblasts. International journal of pharmaceutics *218*, 81-92.
952 Cossart, P., and Helenius, A. (2014). Endocytosis of viruses and bacteria. Cold Spring Harb
953 Perspect Biol *6*.
954 Costa, T.R., Felisberto-Rodrigues, C., Meir, A., Prevost, M.S., Redzej, A., Trokter, M., and
955 Waksman, G. (2015). Secretion systems in Gram-negative bacteria: structural and mechanistic
956 insights. Nat Rev Microbiol *13*, 343-359.
957 Cullis, P.R., and Hope, M.J. (2017). Lipid Nanoparticle Systems for Enabling Gene Therapies.
958 Mol Ther *25*, 1467-1475.
959 de Beer, M., Roverts, R., Heiligenstein, X., Lamers, E., Sommerdijk, N., and Akiva, A. (2021).
960 Visualizing Biological Tissues: A Multiscale Workflow from Live Imaging to 3D Cryo-
961 CLEM. Microscopy and Microanalysis *27*, 11-12.

962 Dell'Era, S., Buchrieser, C., Couve, E., Schnell, B., Briers, Y., Schuppler, M., and Loessner,
963 M.J. (2009). *Listeria monocytogenes* L-forms respond to cell wall deficiency by modifying
964 gene expression and the mode of division. Mol Microbiol *73*, 306-322.
965 Dubnau, D. (1991). Genetic competence in Bacillus subtilis. Microbiological reviews *55*, 395-
966 424.
967 Elkin, S.R., Lakoduk, A.M., and Schmid, S.L. (2016). Endocytic pathways and endosomal
968 trafficking: a primer. Wien Med Wochenschr *166*, 196-204.
969 Ellison, C.K., Dalia, T.N., Vidal Ceballos, A., Wang, J.C., Biais, N., Brun, Y.V., and Dalia,
970 A.B. (2018). Retraction of DNA-bound type IV competence pili initiates DNA uptake during
971 natural transformation in Vibrio cholerae. Nat Microbiol *3*, 773-780.
972 Errington, J. (2013). L-form bacteria, cell walls and the origins of life. Open Biol *3*, 120143.
973 Errington, J., Mickiewicz, K., Kawai, Y., and Wu, L.J. (2016). L-form bacteria, chronic
974 diseases and the origins of life. Phil Trans R Soc B *371*, 20150494.
975 Evers, M.J.W., Kulkarni, J.A., van der Meel, R., Cullis, P.R., Vader, P., and Schiffelers, R.M.
976 (2018). State-of-the-Art Design and Rapid-Mixing Production Techniques of Lipid
977 Nanoparticles for Nucleic Acid Delivery. Small Methods *2*.
978 Forgac, M. (2007). Vacuolar ATPases: rotary proton pumps in physiology and
979 pathophysiology. Nat Rev Mol Cell Biol *8*, 917-929.
980 Forster, B.M., and Marquis, H. (2012). Protein transport across the cell wall of monoderm
981 Gram-positive bacteria. Mol Microbiol *84*, 405-413.
982 Friedrich, A., Hartsch, T., and Averhoff, B. (2001). Natural transformation in mesophilic and
983 thermophilic bacteria: identification and characterization of novel, closely related competence
984 genes in Acinetobacter sp. strain BD413 and Thermus thermophilus HB27. Applied and
985 Environmental Microbiology *67*, 3140-3148.
986 Gilbreath, J.J., Cody, W.L., Merrell, D.S., and Hendrixson, D.R. (2011). Change is good:
987 variations in common biological mechanisms in the epsilonproteobacterial genera
988 Campylobacter and Helicobacter. Microbiol Mol Biol Rev *75*, 84-132.
989 Gregory, M.A., Till, R., and Smith, M.C.M. (2003). Integration site for *Streptomyces* phage
990 phiBT1 and development of site-specific integrating vectors. J Bacteriol *185*, 5320-5323.
991 Hahn, J., Albano, M., and Dubnau, D. (1987). Isolation and characterization of Tn917lac-
992 generated competence mutants of Bacillus subtilis. J Bacteriol *169*, 3104-3109.
993 Hammond, L.R., White, M.L., and Eswara, P.J. (2019). ¡vIVA la DivIVA! J Bacteriol *201*.
994 Hamoen, L.W., Venema, G., and Kuipers, O.P. (2003). Controlling competence in Bacillus
995 subtilis: shared use of regulators. Microbiology (Reading) *149*, 9-17.
996 Han, J., Shi, W., Xu, X., Wang, S., Zhang, S., He, L., Sun, X., and Zhang, Y. (2015). Conditions
997 and mutations affecting *Staphylococcus aureus* L-form formation. Microbiology *161*, 57-66.
998 Hensel, M., Achmus, H., DeckersHebestreit, G., and Altendorf, K. (1996). The ATP synthase
999 of Streptomyces lividans: Characterization and purification of the F1Fo complex. Bba-
1000 Bioenergetics *1274*, 101-108.
1001 Hoffmann, J., and Mendgen, K. (1998). Endocytosis and membrane turnover in the germ tube
1002 of uromyces fabae. Fungal Genet Biol *24*, 77-85.
1003 Hou, X.C., Zaks, T., Langer, R., and Dong, Y.Z. (2021). Lipid nanoparticles for mRNA
1004 delivery. Nat Rev Mater *6*, 1078-1094.
1005 Inamine, G.S., and Dubnau, D. (1995). ComEA, a Bacillus subtilis integral membrane protein
1006 required for genetic transformation, is needed for both DNA binding and transport. J Bacteriol
1007 *177*, 3045-3051.
1008 Jurasek, M., Flardh, K., and Vacha, R. (2020). Effect of membrane composition on DivIVA-
1009 membrane interaction. Biochim Biophys Acta Biomembr *1862*, 183144.
1010 Kieser, T., Bibb, M.J., Buttner, M.J., Chater, K.F., and Hopwood, D.A. (2000). Practical
1011 *Streptomyces* genetics (Norwich: The John Innes Foundation).

Kotnik, T. (2013). Lightning-triggered electroporation and electrofusion as possible contributors to natural horizontal gene transfer. Phys Life Rev *10*, 351-370.
Kruger, N.J., and Stingl, K. (2011). Two steps away from novelty--principles of bacterial DNA uptake. Mol Microbiol *80*, 860-867.
Kulkarni, J.A., Witzigmann, D., Chen, S., Cullis, P.R., and van der Meel, R. (2019). Lipid Nanoparticle Technology for Clinical Translation of siRNA Therapeutics. Accounts Chem Res *52*, 2435-2444.
Lande, M.B., Donovan, J.M., and Zeidel, M.L. (1995). The relationship between membrane fluidity and permeabilities to water, solutes, ammonia, and protons. J Gen Physiol *106*, 67-84.
Lenaz, G. (1987). Lipid fluidity and membrane protein dynamics. Biosci Rep *7*, 823-837.
Li, L., Wan, T., Wan, M., Liu, B., Cheng, R., and Zhang, R. (2015). The effect of the size of fluorescent dextran on its endocytic pathway. Cell Biol Int *39*, 531-539.
Liang, W., and W. Lam, J.K. (2012). Endosomal Escape Pathways for Non-Viral Nucleic Acid Delivery Systems. In Molecular Regulation of Endocytosis.
MacNeil, D.J., Gewain, K.M., Ruby, C.L., Dezeny, G., Gibbons, P.H., and MacNeil, T. (1992). Analysis of *Streptomyces avermitilis* genes required for avermectin biosynthesis utilizing a novel integration vector. Gene *111*, 61-68.
Mercier, R., Kawai, Y., and Errington, J. (2013). Excess membrane synthesis drives a primitive mode of cell proliferation. Cell *152*, 997-1007.
Mulkidjanian, A.Y., Makarova, K.S., Galperin, M.Y., and Koonin, E.V. (2007). Inventing the dynamo machine: the evolution of the F-type and V-type ATPases. Nat Rev Microbiol *5*, 892-899.
Munch, B., Trtik, P., Marone, F., and Stampanoni, M. (2009). Stripe and ring artifact removal with combined wavelet - Fourier filtering. Opt Express *17*, 8567-8591.
Muschiol, S., Balaban, M., Normark, S., and Henriques-Normark, B. (2015). Uptake of extracellular DNA: competence induced pili in natural transformation of *Streptococcus pneumoniae*. Bioessays *37*, 426-435.
Nishida, H. (2020). Factors That Affect the Enlargement of Bacterial Protoplasts and Spheroplasts. Int J Mol Sci *21*.
Oparka, K.J., Wright, K.M., Murant, E.A., and Allan, E.J. (1993). Fluid-Phase Endocytosis - Do Plants Need It. J Exp Bot *44*, 247-255.
Patel, S., Kim, J., Herrera, M., Mukherjee, A., Kabanov, A.V., and Sahay, G. (2019). Brief update on endocytosis of nanomedicines. Adv Drug Deliv Rev *144*, 90-111.
Perona, P., and Malik, J. (1990). Scale-Space and Edge-Detection Using Anisotropic Diffusion. Ieee T Pattern Anal *12*, 629-639.
Ramijan, K., Ultee, E., Willemse, J., Zhang, Z., Wondergem, J.A.J., van der Meij, A., Heinrich, D., Briegel, A., van Wezel, G.P., and Claessen, D. (2018). Stress-induced formation of cell wall-deficient cells in filamentous actinomycetes. Nat Commun *9*, 5164.
Ramijan, K., van Wezel, G.P., and Claessen, D. (2017). Genome sequence of the filamentous actinomycete *Kitasatospora viridifaciens*. Genome Announc *5*, e01560-01516.
Roberts, J., and Park, J.S. (2004). Mfd, the bacterial transcription repair coupling factor: translocation, repair and termination. Current Opinion in Microbiology *7*, 120-125.
Sato, K., Nagai, J., Mitsui, N., Ryoko, Y., and Takano, M. (2009). Effects of endocytosis inhibitors on internalization of human IgG by Caco-2 human intestinal epithelial cells. Life Sci *85*, 800-807.
Scheinpflug, K., Krylova, O., and Strahl, H. (2017). Measurement of Cell Membrane Fluidity by Laurdan GP: Fluorescence Spectroscopy and Microscopy. Methods Mol Biol *1520*, 159-174.

Schindelin, J., Arganda-Carreras, I., Frise, E., Kaynig, V., Longair, M., Pietzsch, T., Preibisch, S., Rueden, C., Saalfeld, S., Schmid, B., *et al.* (2012). Fiji: an open-source platform for biological-image analysis. Nat Methods *9*, 676-682.

Shimoni, E., and Muller, M. (1998). On optimizing high-pressure freezing: from heat transfer theory to a new microbiopsy device. J Microsc *192*, 236-247.

Shitut, S., Shen, M.-J., Claushuis, B., Derks, R.J.E., Giera, M., Rozen, D., Claessen, D., and Kros, A. (2021). Generating heterokaryotic cells via bacterial cell-cell fusion. BioRxiv.

Spehner, D., Steyer, A.M., Bertinetti, L., Orlov, I., Benoit, L., Pernet-Gallay, K., Schertel, A., and Schultz, P. (2020). Cryo-FIB-SEM as a promising tool for localizing proteins in 3D. J Struct Biol *211*, 107528.

Studer, D., Michel, M., and Muller, M. (1989). High pressure freezing comes of age. Scanning Microscopy *3*, 253-268; discussion 268.

Studer, P., Staubli, T., Wieser, N., Wolf, P., Schuppler, M., and Loessner, M.J. (2016). Proliferation of *Listeria monocytogenes* L-form cells by formation of internal and external vesicles. Nat Commun *7*, 13631.

Stülke, J., Eilers, H., and Schmidl, S.R. (2009). Mycoplasma and spiroplasma. In Encyclopedia of microbiology, M. Schaechter, ed. (Oxford: Elsevier), pp. 208-219.

Stuttard, C. (1982). Temperate phages of *Streptomyces venezuelae*: lysogeny and host specificity shown by phages SV1 and SV2. J Gen Microbiol *128*, 115-121.

Subramanya, S., Hardin, C.F., Steverding, D., and Mensa-Wilmot, K. (2009). Glycosylphosphatidylinositol-specific phospholipase C regulates transferrin endocytosis in the African trypanosome. Biochem J *417*, 685-694.

Takahashi, S., Mizuma, M., Kami, S., and Nishida, H. (2020). Species-dependent protoplast enlargement involves different types of vacuole generation in bacteria. Sci Rep *10*, 8832.

Thomas, C.M., and Nielsen, K.M. (2005). Mechanisms of, and barriers to, horizontal gene transfer between bacteria. Nat Rev Microbiol *3*, 711-721.

Thottacherry, J.J., Sathe, M., Prabhakara, C., and Mayor, S. (2019). Spoiled for Choice: Diverse Endocytic Pathways Function at the Cell Surface. Annu Rev Cell Dev Bi *35*, 55-84.

Trombone, A.P., Silva, C.L., Lima, K.M., Oliver, C., Jamur, M.C., Prescott, A.R., and Coelho-Castelo, A.A. (2007). Endocytosis of DNA-Hsp65 alters the pH of the late endosome/lysosome and interferes with antigen presentation. PLoS One *2*, e923.

Varkouhi, A.K., Scholte, M., Storm, G., and Haisma, H.J. (2011). Endosomal escape pathways for delivery of biologicals. J Control Release *151*, 220-228.

Vidavsky, N., Akiva, A., Kaplan-Ashiri, I., Rechav, K., Addadi, L., Weiner, S., and Schertel, A. (2016). Cryo-FIB-SEM serial milling and block face imaging: Large volume structural analysis of biological tissues preserved close to their native state. J Struct Biol *196*, 487-495.

Vischer, N. (2016). Using ImageJ to show "Generalized Polarization" (GP).

Woese, C. (1998). The universal ancestor. P Natl Acad Sci USA *95*, 6854-6859.

Woese, C.R. (2000). Interpreting the universal phylogenetic tree. P Natl Acad Sci USA *97*, 8392-8396.

Wolff, J.A., and Budker, V. (2005). The Mechanism of Naked DNA Uptake and Expression. Adv Genet *54*, 3-20.

Wolff, J.A., Malone, R.W., Williams, P., Chong, W., Acsadi, G., Jani, A., and Felgner, P.L. (1990). Direct Gene-Transfer into Mouse Muscle Invivo. Science *247*, 1465-1468.

Wolfgang, M., van Putten, J.P.M., Hayes, S.F., and Koomey, M. (1999). The comP locus of Neisseria gonorrhoeae encodes a type IV prepilin that is dispensable for pilus biogenesis but essential for natural transformation. Molecular Microbiology *31*, 1345-1357.

Wu, C., van der Heul, H.U., Melnik, A.V., Lubben, J., Dorrestein, P.C., Minnaard, A.J., Choi, Y.H., and van Wezel, G.P. (2019). Lugdunomycin, an Angucycline-Derived Molecule with Unprecedented Chemical Architecture. Angew Chem Int Ed Engl *58*, 2809-2814.

1110 Yabu, K. (1991). Formation of Vesiculated Large Bodies of Staphylococcus-Aureus L-Form
1111 in a Liquid-Medium. Microbiology and Immunology *35*, 395-404.
1112 Yanisch-Perron, C., Vieira, J., and Messing, J. (1985). Improved M13 phage cloning vectors
1113 and host strains: nucleotide sequences of the M13mp18 and pUC19 vectors. Gene *33*, 103-119.
1114 Yeh, Y.C., Lin, T.L., Chang, K.C., and Wang, J.T. (2003). Characterization of a ComE3
1115 homologue essential for DNA transformation in Helicobacter pylori. Infect Immun *71*, 5427-
1116 5431.
1117 Zacchetti, B., Smits, P., and Claessen, D. (2018). Dynamics of pellet fragmentation and
1118 aggregation in liquid-grown cultures of *Streptomyces lividans*. Front Microbiol *9*, 943.
1119 Zacchetti, B., Willemse, J., Recter, B., van Dissel, D., van Wezel, G.P., Wösten, H.A.B., and
1120 Claessen, D. (2016). Aggregation of germlings is a major contributing factor towards mycelial
1121 heterogeneity of *Streptomyces*. Sci Rep *6*, 27045.
1122 Zhang, L., Ramijan, K., Carrion, V.J., van der Aart, L.T., Willemse, J., van Wezel, G.P., and
1123 Claessen, D. (2021). An alternative and conserved cell wall enzyme that can substitute for the
1124 lipid II synthase MurG. mBio *12*.
1125 Zuiderveld, K. (1994). Contrast limited adaptive histogram equalization. Graphics gems, 474-
1126 485.
1127

1128

SUPPLEMENTAL TABLES

Table S1. BlastP results showing significant hits (E-value < 1e-06), E-value and percent identity against *K. viridifaciens* DSM40239.

Organism	Protein name	Hits	E-value	Percent identity
Bacillus subtilis strain 168	ComEA	BOQ63_29625	5.28e-24	34.90%
	ComEC	BOQ63_29630	1.78e-09	26.81%
	ComFA	BOQ63_20315	1.03e-07	24.83%
	ComGA, ComGB, ComGC, ComGD, ComGE, ComGF, ComGG, ComC	-	-	
Neisseria gonorrhoeae	ComE	BOQ63_29625	4.05e-10	46.43%
	ComA, ComP*, PilC, PilD, PilE, PilV, PilQ, PilF, PilG, PilT	-	-	
Helicobacter pylori strain P12	ComE3 (ComEC), ComB2-4, Com6-10	-	-	

*Protein sequence obtained from Wolfgang et al. (1999)

1133 **Table S2.** Strains used in this study.

Strain	Description	Notes/references
Escherichia coli JM109	*recA*1, *endA*1, *gyrA*96, *thi*, *hsdR*17, *supE*44, *relA*1, λ⁻, Δ (*lac-proAB*), [F', *traD*36 *proAB*, *lacI*^{q}ZΔM15]	Yanisch-Perron et al. (1985)
Escherichia coli ET12567/pUZ8002	Methylation-deficient strain (F⁻, *dam*-13::*Tn*9, *dcm*-6, *hsdM*, *hsdR*, *recF*143, *zjj*-202::Tn10, *galK*2, *galT*22, *ara*14, *lacY*1, *xyl*-5, *leuB*6, *thi*-1, *tonA*31, *rpsL*136, *hisG*4, *tsx*-78, *mtl*-1, *glnV*44) carrying the non-transmissible pUZ8002 plasmid	MacNeil et al. (1992)
Kitasatospora viridifaciens DSM40239	Wild-type strain	DSMZ, Ramijan et al. (2017)
alpha	L-form derivative of DSM40239 obtained after exposure to Penicillin G and lysozyme	Ramijan et al. (2018)
M1	L-form derivative of DSM40239 obtained after exposure to hyperosmotic stress	Ramijan et al. (2018)
delta	L-form derivative of DSM40239 obtained after exposure to Penicillin G and lysozyme	Shitut et al. (2021)
alpha pIJ82-GFP	*alpha* containing pIJ82-GFP	This work
alpha pKR2	*alpha* containing pKR2, which contains a C-terminal eGFP gene fusion to *divIVA* under the control of the *S. coelicolor gap1* promoter	Zhang et al. (2021)
*alpha*Δ*divIVA*	*divIVA::aac(3)IV*	Zhang et al. (2021)
*alpha*Δ*divIVA* pIJ82-GFP	*alpha*Δ*divIVA* containing pIJ82-GFP	This work
*alpha*Δ*ssgB*	*ssgB::aac(3)IV*	Ramijan et al. (2018)
*alpha*Δ*comEA/EC*	*(comEA-comEC)::aac(3)IV*	This work

1134 **Table S3**. Plasmids used in this study.

Plasmid	Features	Notes/References
pRed*	pIJ8630-derivative expressing *mCherry* under control of the *S. coelicolor A3(2) gap1* promoter	Zacchetti et al. (2018)
pGreen	pIJ8630-derivative expressing *eGFP* under control of the *S. coelicolor A3(2) gap1* promoter	Zacchetti et al. (2016)
pSET152	*E. coli-Streptomyces* shuttle vector; high copy number in *E. coli* and integrating in the ϕC31 *attB* site in *Streptomyces*	Bierman et al. (1992)
pIJ82	pSET152-derivative carrying a hygromycin resistance cassette	Kindly provided by Dr. B. Gust (JIC)
pIJ82-GFP	pSET152-derivative expressing *eGFP* under control of the *S. coelicolor gap1* promoter	This work
pMS82	*E. coli-Streptomyces* shuttle vector integrative in the ϕBT1 *attB* site for genomic integration in *Streptomyces*	Gregory et al. (2003)
pWHM3-oriT	Self-replicating, multi-copy, unstable plasmid harboring *oriT,* used as *E. coli/Streptomyces* shuttle vector	Wu et al. (2019)
pWHM3-oriT-hyg	pWHM3-oriT-derivative carrying a hygromycin resistance cassette inserted in to the *tsr* gene in the EcoRV site	This work
pFL-*ssgB*	pWHM3-oriT-hyg-derivative containing a hygromycin resistance gene and a downstream flanking sequence of *ssgB* downstream derived from pKR1 to enable integration into the genome	This work

pRK1	pWHM3-oriT containing both flanks of the *comEA-comEC* region interspersed with the *apra-loxP* cassette conferring resistance to apramycin	This work
pKR1	pWHM3-based construct used to replace *ssgB* by *aac(3)IV*	Ramijan et al. (2018)
pKR2	pIJ8630 derivative carrying a viomycin resistance cassette and expressing a C-terminal *eGFP* fusion to *divIVA* under control of the *S. coelicolor* A3(2) *gap1* promoter	Zhang et al. (2021)

1137 **Table S4.** Primers used in this study.

Primer	Sequence (5' - 3')	Notes	Reference
Hyg_F-231_EEV	ctgaGAATTCGATATCGATCG GCGGGGCCTGGCGGCG	Amplification of the hygromycin resistance cassette from pMS82	This work
Hyg_R+1237_HEV	ctgaAAGCTTGATATCGGATC CTTGCCGAGCTGGGAT	Amplification of the hygromycin resistance cassette from pMS82	This work
FL1-comEA/comEC-FW	GACGAATTCAGGACCGGAT GCACCGGTTC	Amplification of flank 1 of *comEA-comEC* locus	This work
FL1-comEA/comEC-REV	GAATCTAGACCGCACCGTCT CGTTGATCG	Amplification of flank 1 of *comEA-comEC* locus	This work
ComEA_Apra_check_FW	CACTCGTGTGAGTGACCGTT	Amplification of *comEA* region in PCR1 mix	This work
ComEC_Apra_check_RV	AACGGCAAGGGTGGACG	Amplification of *comEA* region in PCR1 mix	This work
ComEC_Presence_Check_1_FW	TACGACACCGAGTCCGCAG	Amplification of *comEC* region 1 in PCR2 mix	This work
ComEC_Presence_Check_1_RV	CGCAAGGGCCAACATGTCTC	Amplification of *comEC* region 1 in PCR2 mix	This work
ComEC_Presence_Check_2_FW	AGACCCTCCTCACCGTCAAG	Amplification of *comEC* region 2 in PCR2 mix	This work
ComEC_Presence_Check_2_RV	GACAGCAGGAAACCGAAGG A	Amplification of *comEC* region 2 in PCR2 mix	This work
gap1_FW_BglII	GATTACAGATCTCCGAGGGC TTCGAGACC	Amplification of the region containing the *gap1* promoter and *eGFP* gene from pGreen	This work

egfp_RV_EcoRI	TAAGCAGAATTCTTACTTGT ACAGCTCGTCCA	Amplification of the region containing the *gap1* promoter and *eGFP* gene from pGreen	This work
SsgB_Presence_FW	GGCGGGTACTCCGTGATGAT TC	Confirmation of *ssgB* replacement by *apra-loxP* cassette	This work
SsgB_Presence_RV	AGCTTTCGGCGAGGATGTGG	Confirmation of *ssgB* replacement by *apra-loxP* cassette	This work
Tsr_Hyg_FW1	AAGGCCAAGACATTCGGCAT	Confirmation of presence of pFL-*ssgB* in natural transformants	This work
Tsr_Hyg_RV1	CGAGCGACGTGCGTACTATC	Confirmation of presence of pFL-*ssgB* in natural transformants	This work

1138

1139

1140 **Table S5**. Imaging settings used with the Zeiss LSM 900 confocal microscope.

Fluorescent dye or particle	Excitation (nm)	Emission filter (nm)
eGFP	488	490-575
mCherry	561	565-700
SYTO-9	488	490-575
SynapseRed C2M	506	571-700
Dextran-Texas Red	584	560-700
Cy5	650	450-700
LNP-LR	587	565-700

1141
1142

1143 **Table S6.** Dynamic Light Scattering (DLS) and ζ-potential of lipid nanoparticles. PDI =

1144 polydispersity index.

LNP	Avg. size (nm) at 25 °C	PDI	ζ-potential at 25 °C
LNP-LR	125.8	0.126	-8.5

1145

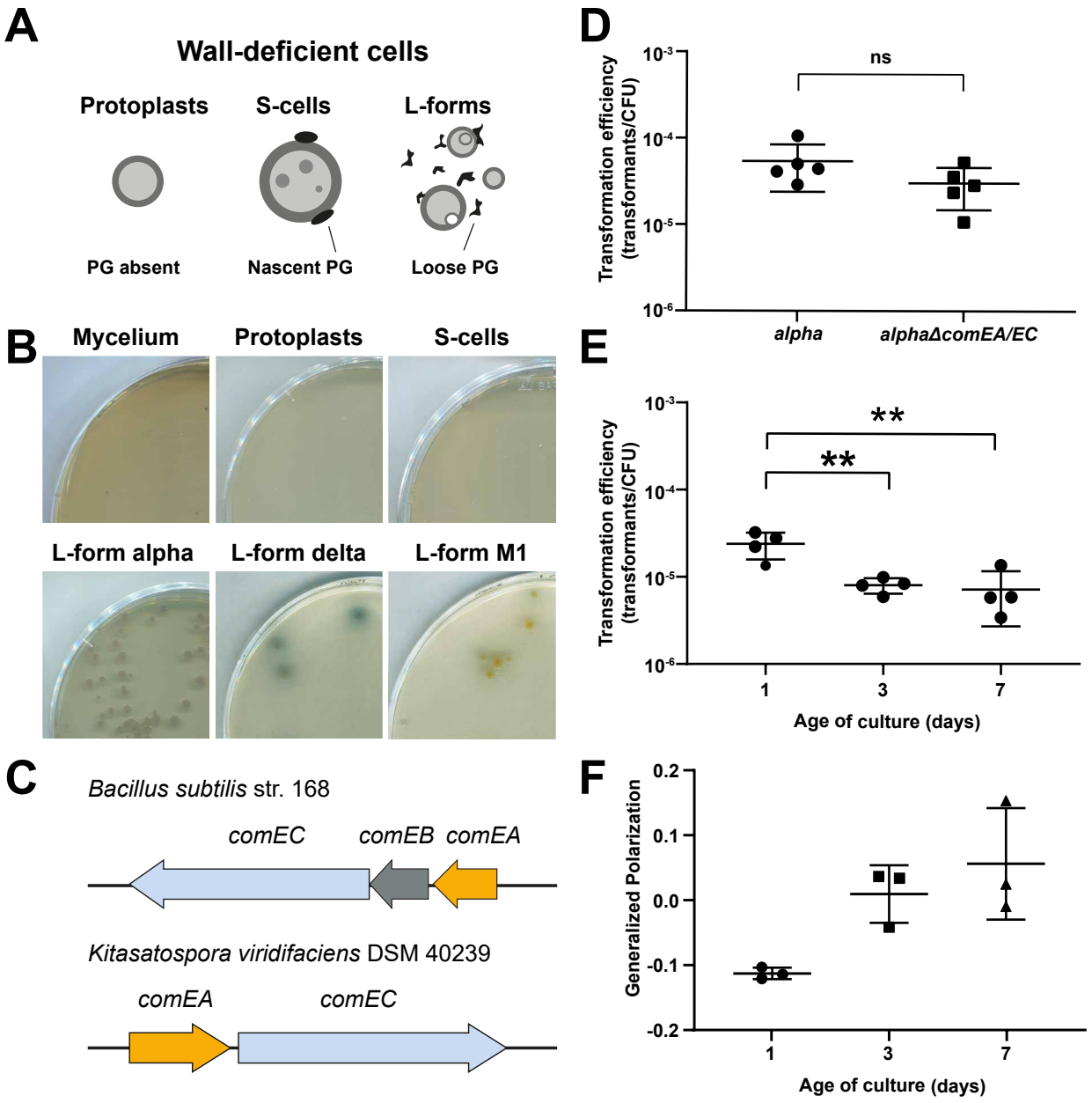

Figure 1. Natural DNA Uptake of Wall-Deficient Cells Is Independent of the Competence Proteins ComEA and ComEC and Correlates with Membrane Fluidity

(A) Schematic representation of the different wall-deficient cell types of *K. viridifaciens* that can be created artificially (protoplasts) or naturally (S-cells and L-forms). PG = peptidoglycan.

(B) Mycelium, protoplasts, S-cells and L-form lines *alpha*, M1 and *delta* were incubated with plasmid DNA (pRed*) for 24h, plated on selective medium and incubated at 30°C to select for transformed cells. Note that only L-forms show consistent DNA uptake.

(C) Localization of putative ComEA and ComEC genes (BOQ63_29625 and BOQ63_29630, respectively) on the chromosome of *K. viridifaciens* DSM 40239 as compared to *comEC* and *comEA* of naturally transformable *Bacillus subtilis* str. 168.

(D) Natural transformation assay of 7-day of alpha and *alphaΔcomEA/EC* using pFL-*ssgB*. ns = not significant (n=5 replicates, two-tailed independent t-test, t(8)=1.572, P=0.155). Data are represented as mean ±SD with individual data points.

(E) Natural transformation efficiency of 1-, 3- and 7-day old alpha after 24 h incubation with pFL-ssgB. Asterisks indicate statistically significant different transformation efficiency (n=4 replicates, one-way ANOVA, F (2,9) = 12.16, Tukey post-hoc test, P =.006 (1-3 day) and .005 (1-7 day)). Data are represented as mean ±SD with individual data points.

(F) Generalized polarization as measurement of membrane fluidity of 1-, 3- and 7-day old alpha as calculated from the shift in the fluorescence emission spectrum of the membrane dye Laurdan. Lower GP indicates a higher membrane fluidity. Data are represented as mean ±SD with individual data points, n=3.

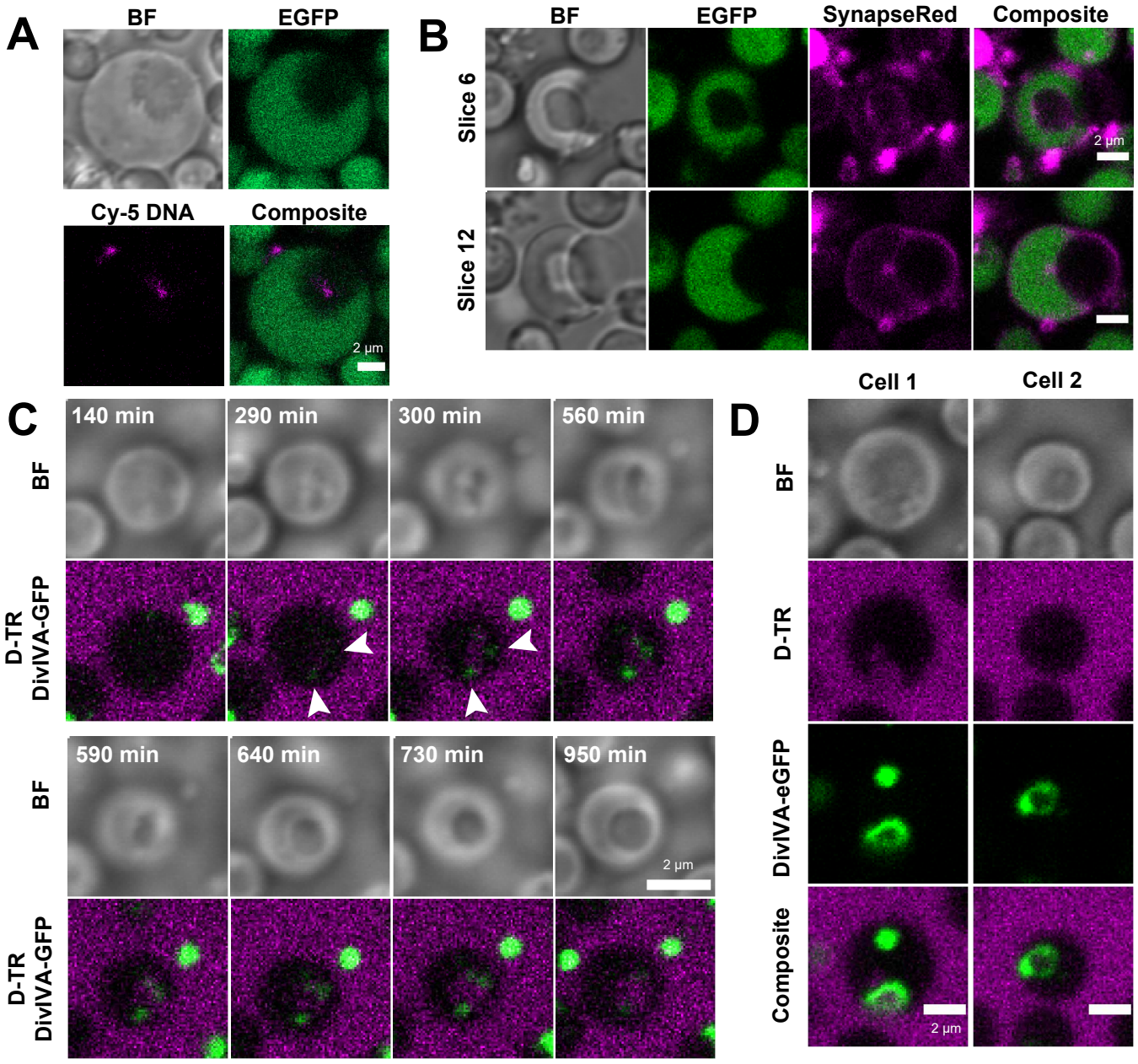

Figure 2. Formation of Internal Vesicles and Uptake of External Fluids in L-forms

(A) Fluorescence micrograph of *alpha* pIJ82-GFP (cytoplasmic eGFP; green) incubated with Cy-5 labelled plasmid DNA (pFL-*ssgB*; magenta). BF = Brightfield. Scale bar = 2 µm.

(B) Incubation of *alpha* pIJ82-GFP with the membrane-impermeable dye SynapseRed C2M (SynapseRed; magenta), showing two z-slices of one L-form cell. BF = brightfield. Scale bar = 2µm.

(C) Stills of a time-lapse imaging experiment of *alpha* producing DivIVA-eGFP (*alpha* pKR2) (green) incubated with 3 kDa Dextran-Texas Red (D-TR; magenta). Arrows indicate localization of DivIVA-eGFP. Scale bar = 2µm. See also Video S1.

(D) Formation of foci and ring-structures of DivIVA-eGFP in *alpha* pKR2 (green) incubated with Dextran-Texas Red (D-TR, magenta). Scale bar = 2µm. Note that L-forms are able to take up fluorescently stained DNA and Dextran by formation of internal vesicles.

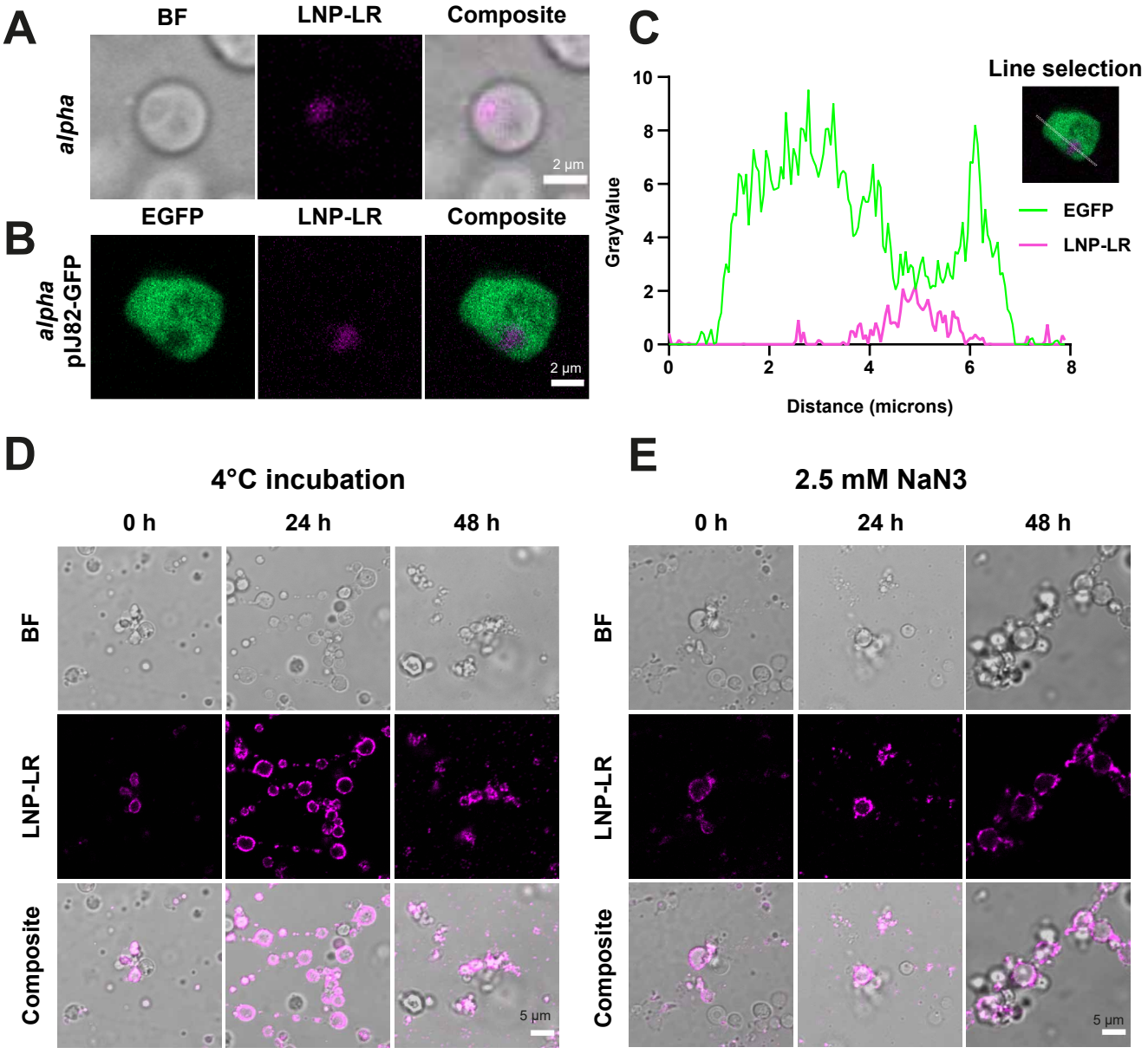

Figure 3. Localization of Lipid Nanoparticles in Internal L-form Vesicles

(A-B) Localization of LNP-LR (Lipid Nanoparticle containing 18:1 Liss Rhod PE; magenta) in internal vesicles of *alpha* (A) and *alpha* pIJ82-GFP (B) after overnight or 3-day incubation at 30°C respectively. Scale bar = 2µm.

(C) Density profile plot and corresponding line selection of *alpha* pIJ82-GFP incubated with LNP-LR showing a decrease in cytoplasmic eGFP emission correlates with an increase in LNP-LR emission.

(D-E) Localization of LNP-LR during incubation with *alpha* at 4°C (D) or in the presence of 2.5 mM sodium azide at 30°C (E) after 0, 24 and 48 h incubation. Similar results were obtained with 1 and 10 mM sodium azide (data not shown). Scale bar = 5 µm. Note that incubation of L-forms with lipid nanoparticles (average size of 125 nm) results in their localization inside internal vesicles, a process that can be inhibited by incubation at 4°C or sodium azide.

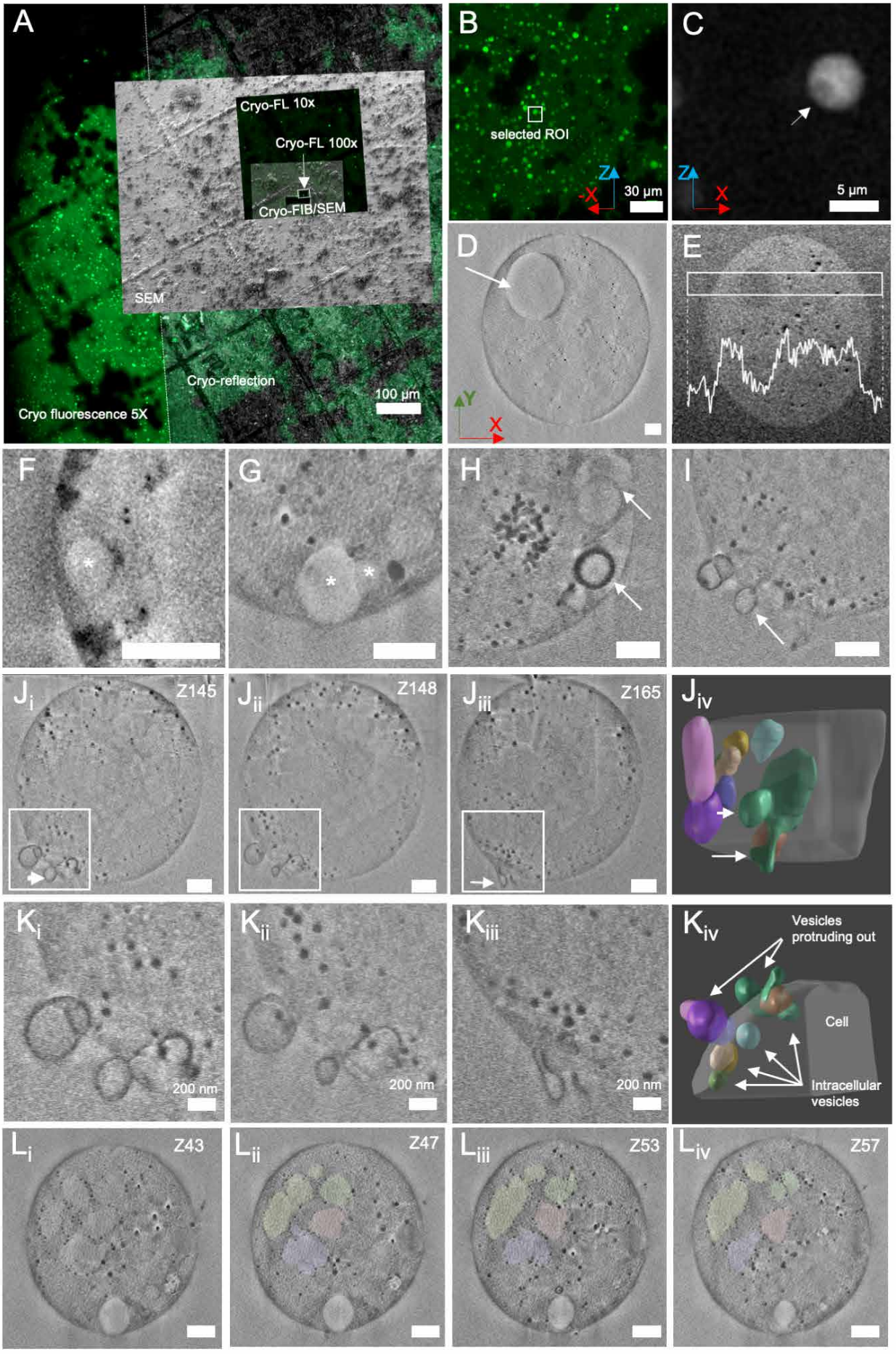
A
Cryo-FL 10x
Cryo-FL 100x
Cryo-FIB/SEM
SEM
Cryo-reflection
100 µm
Cryo fluorescence 5X
B
selected ROI
Z
X
30 µm
C
Z
X
5 µm
D
Y
X
E
F
G
H
I
J_i
Z145
J_ii
Z148
J_iii
Z165
J_iv
K_i
200 nm
K_ii
200 nm
K_iii
200 nm
K_iv
Vesicles protruding out
Cell
Intracellular vesicles
L_i
Z43
L_ii
Z47
L_iii
Z53
L_iv
Z57

Figure 4. 3D Cryo-Fluorescence and Cryo-FIB-SEM of L-forms Reveals its Ultra-Structure in High Resolution

(A) Correlated fluorescence and electron micrographs of the frozen sample (Zen Connect image). The bright green dots indicate individual cells of *alpha* pIJ82-GFP. A finderTOP raster visible both in fluorescence and electron microscopy facilitates alignment between the two imaging modules. The small squares indicate different regions of interest, imaged at higher resolution. FL: Fluorescence light

(B) Higher resolution image of one region of interest, showing many fluorescent cells.

(C) L-form depicted by white box in B, showing intracellular dark sphere (~ 1 micrometer, white arrow).

(D) SEM image (SE, Inlens) of cell in C) with white arrow indicating the internal vesicle. The X, Y and Z arrows in B, C and D indicate the 3D orientation of the imaged cell as observed in 3D FIB-SEM.

(E) Superposition of five consecutive slices (backscattered images) of cell in D). Inset: Intensity plot profile (white) of the region in white box.

(F-I) FIB-SEM slices showing different types of internal vesicles. (F-G) Vesicles lining the cell membrane. Asterisks indicate vesicles. (H) Vesicle complex, note the different membrane thickness of vesicles indicated with white arrows. See also Figure S6D and Video S3. (I) Membrane protrusions as indicated with white arrow.

(J-K) Analysis of the interconnected vesicles of the cell in I). (Ji-iii) Three consecutive slices showing the interaction of different vesicles. Ki-iii show higher magnification of the regions in white boxes in Ji-iii, respectively). (Jiv, Kiv) 3D segmentation of Ki-iii. While some of the vesicles are intracellular, others protrude out of the cell. A complete connected vesicle structure is shown in green and is indicated by white arrows in I, Jiii and Jiv. See also Figure S6A-C and Video S2.

(L) Regions with different contrast are lined with black particles representing putative lipid bodies. The size distribution of the black particles is between 25 to 60 nm. Scale bars represent 500 nm unless otherwise specified.

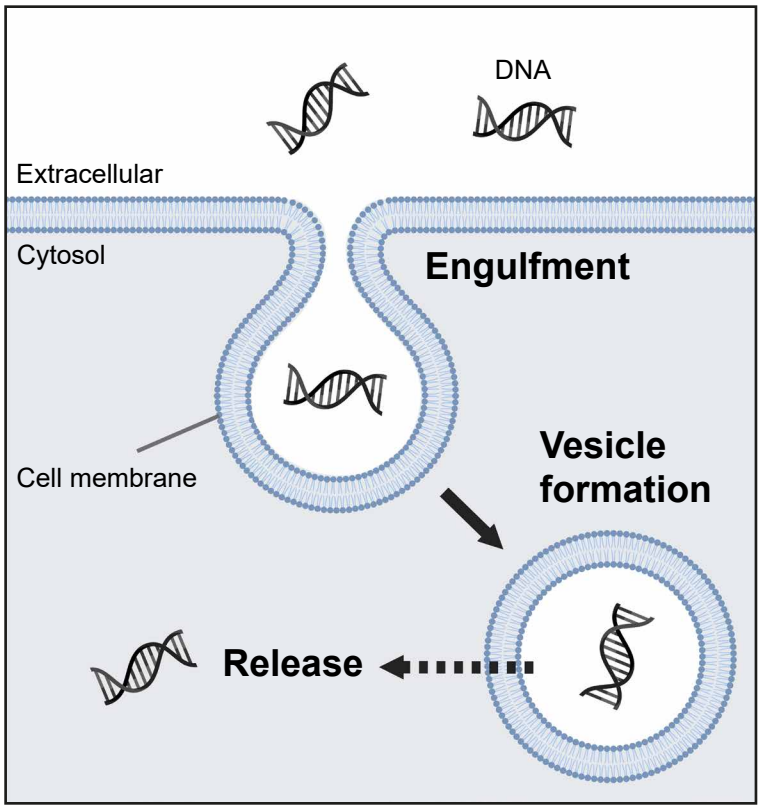

Figure 5. Proposed Model for DNA Uptake by Internal Vesicle Formation in L-forms
Excess membrane synthesis results in invagination of the cell membrane, leading to the formation of internal vesicles in L-forms. In this process, extracellular liquid containing DNA or other macromolecules is engulfed. Finally, DNA is released from internal vesicles by an unknown process (indicated by dashed arrow), which may involve vesicle disruption. Image created with BioRender.com.

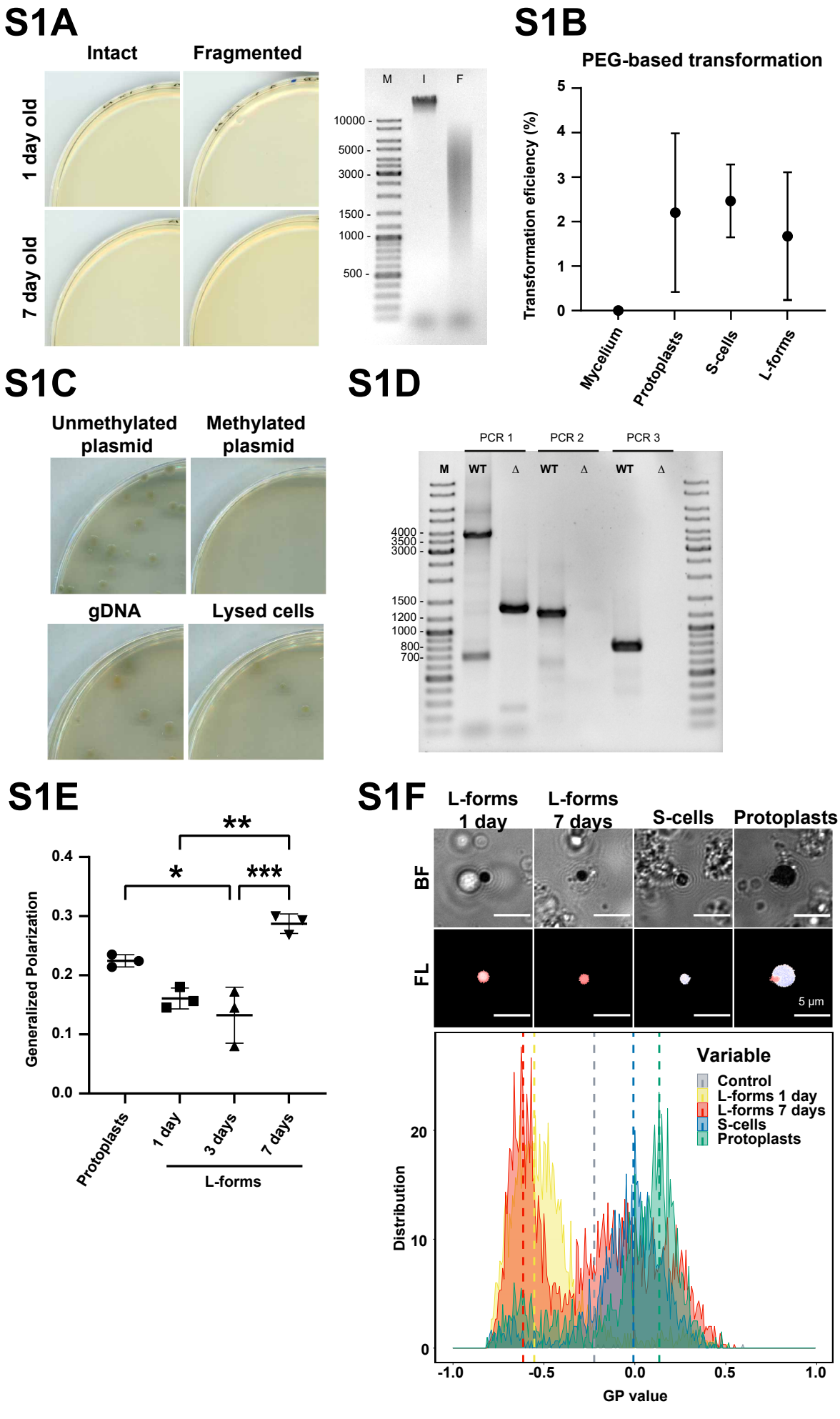
S1A
Intact
Fragmented
1 day old
7 day old
M
I
F
10000
5000
3000
1500
1000
500
S1B
PEG-based transformation
Transformation eficiency (%)
0
1
2
3
4
5
Mycelium
Protoplasts
S-cells
L-forms
S1C
Unmethylated plasmid
Methylated plasmid
gDNA
Lysed cells
S1D
PCR 1
PCR 2
PCR 3
M
WT
Δ
WT
Δ
WT
Δ
4000
3500
3000
1500
1200
1000
800
700
S1E
Generalized Polarization
0.0
0.1
0.2
0.3
0.4
*
**
***
Protoplasts
1 day
3 days
7 days
L-forms
S1F
L-forms 1 day
L-forms 7 days
S-cells
Protoplasts
BF
FL
5 µm
Variable
Control
L-forms 1 day
L-forms 7 days
S-cells
Protoplasts
Distribution
0
10
20
-1.0
-0.5
0.0
0.5
1.0
GP value

Figure S1. Analysis of Natural and Artificial DNA Uptake and Membrane Fluidity of Cell-Wall Deficient Cells and Confirmation of alphaΔcomEA/EC Mutant, Related to Figure 1

(A) (Left) Transformation plates showing absence of natural transformation upon incubation of 1-and 7-day old L-form alpha with intact or fragmented gDNA of *alphaΔssgB* containing an apramycin resistance cassette. (Right) Gel electrograph of 100 ng intact (I) or fragmented (F) gDNA of *alphaΔssgB* as used in the natural transformation assay.

(B) Polyethylene glycol (PEG)-based transformation efficiency of *K. viridifaciens* mycelium, protoplasts, S-cells and L-forms using plasmid DNA (pRed*) containing an apramycin resistance gene, shown as the percentage of transformed colonies per total colony forming units. Data are represented as mean ± SD, n=3.

(C) PEG-based transformation of alpha using unmethylated or methylated plasmid DNA (pRed*), gDNA or filter-sterilized salt-lysed cells from mutant line *alphaΔssgB*.

(D) Gel electrograph of PCR products from three different PCR mixes to confirm the replacement of *comEA* and *comEC* by an apramycin resistance cassette. WT = gDNA *alpha*; Δ = gDNA *alphaΔcomEA/EC*. Expected products: PCR 1 WT = 3676 bp, mutant = 1294 bp; PCR 2 WT = 1197 bp, mutant = no amplification, PCR 3 WT = 745 bp, mutant = no amplification.

(E) Generalized Polarization (GP) as measure of membrane fluidity of *K. viridifaciens* protoplasts, 1-, 3- and 7- day old L-form *alpha*. Lower GP indicates higher fluidity. *, ** and *** indicate $P \leq 0.05$, 0.01 and 0.001, respectively (one-way ANOVA, $F(3,8) = 19.49$, Tukey post-hoc test, n=3). Data are represented as mean ±SD with individual data points, n=3.

(F) Membrane fluidity of L-form *alpha* (1- and 7-day old), S-cells and protoplasts of *K. viridifaciens*. Top rows show brightfield images and heatmap of fluorescence emission (red to blue colour indicate GP values of -1.0 to 1.0 respectively) of representative cells stained with a Laurdan dye for quantifying the membrane fluidity (BF = brightfield, FL = fluorescence emission). Bottom panel shows frequency distributions of the Generalized Polarization (GP). Lower GP values correspond to higher membrane fluidity indicating that L-forms have more fluid membranes compared to S-cells and protoplasts. Control = cells imaged and analysed without Laurdan staining.

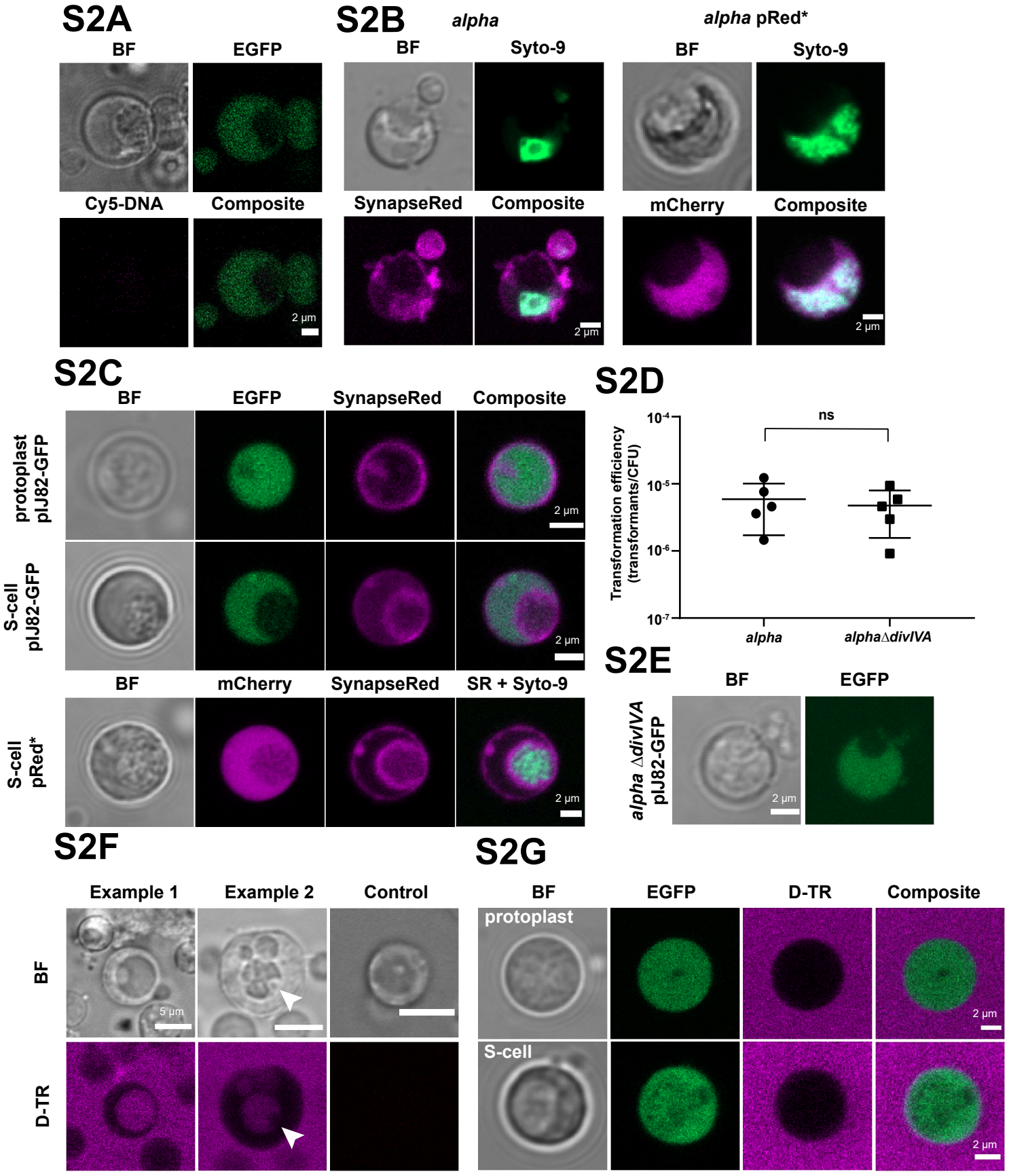
S2A
BF
EGFP
Cy5-DNA
Composite
2 µm
S2B
alpha
BF
Syto-9
SynapseRed
Composite
2 µm
alpha pRed*
BF
Syto-9
mCherry
Composite
2 µm
S2C
BF
EGFP
SynapseRed
Composite
protoplast pIJ82-GFP
S-cell pIJ82-GFP
2 µm
BF
mCherry
SynapseRed
SR + Syto-9
S-cell pRed*
2 µm
S2D
ns
Transformation efficiency (transformants/CFU)
10-4
10-5
10-6
10-7
alpha
alphaΔdivIVA
S2E
BF
EGFP
alpha ΔdivIVA pIJ82-GFP
2 µm
S2F
Example 1
Example 2
Control
BF
D-TR
5 µm
S2G
BF
EGFP
D-TR
Composite
protoplast
S-cell
2 µm
2 µm

Figure S2. Analysis of DNA Content, Internal Vesicles and Uptake of D-TR of Cell-Wall Deficient Cells, and effect of divIVA deletion on DNA Uptake, Related to Figure 2

(A) *alpha* pIJ82-GFP incubated without Cy-5 DNA as fluorescence control.

(B) *alpha* and *alpha* pRed* stained with SYTO-9 (green) to indicate chromosomal DNA. *alpha* is stained with SynapseRed C2M (SynapseRed; magenta) to visualize cell membranes, whereas (absence of) cytosolic mCherry for *alpha* pRed* (magenta) indicates the presence of an internal vesicle.

(C) Protoplasts and S-cells of *K. viridifaciens* pIJ82-GFP producing cytosolic eGFP incubated with SynapseRed for 72 h (top rows), and S-cells of *K. viridifaciens* pRed* producing cytosolic mCherry incubated with SynapseRed (SR) and SYTO-9 for 72 h (bottom row). Chromosomal DNA is visualized using SYTO-9 staining. Note that presence of internal membrane structures causes a reduction in cytosolic fluorescence emission.

(D) Natural transformation assay of 7-day old *alpha* and *alphaΔdivIVA* using pFL-*ssgB*. ns = not significant (two-tailed independent t-test, $t(8)=0.489$, $P=0.638$). Data are represented as mean ± SD with individual data points, n=5.

(E) L-forms without DivIVA can produce internal vesicles as shown for 5-day old *alphaΔdivIVA* pIJ82-GFP producing cytosolic eGFP. Scale bar = 2 μm.

(F) *alpha* incubated with (example 1 and 2) or without (control) Dextran Texas-Red (D-TR; magenta), showing the formation of internal vesicles filled with D-TR. The arrow indicates the presence of a non-fluorescent secondary internal vesicle inside an existing internal vesicle (example 2). Scale bar = 5 μm.

(G) Protoplasts and S-cells of *K. viridifaciens* pIJ82-GFP incubated with D-TR for 72 h. Note that no internalization of D-TR was observed.

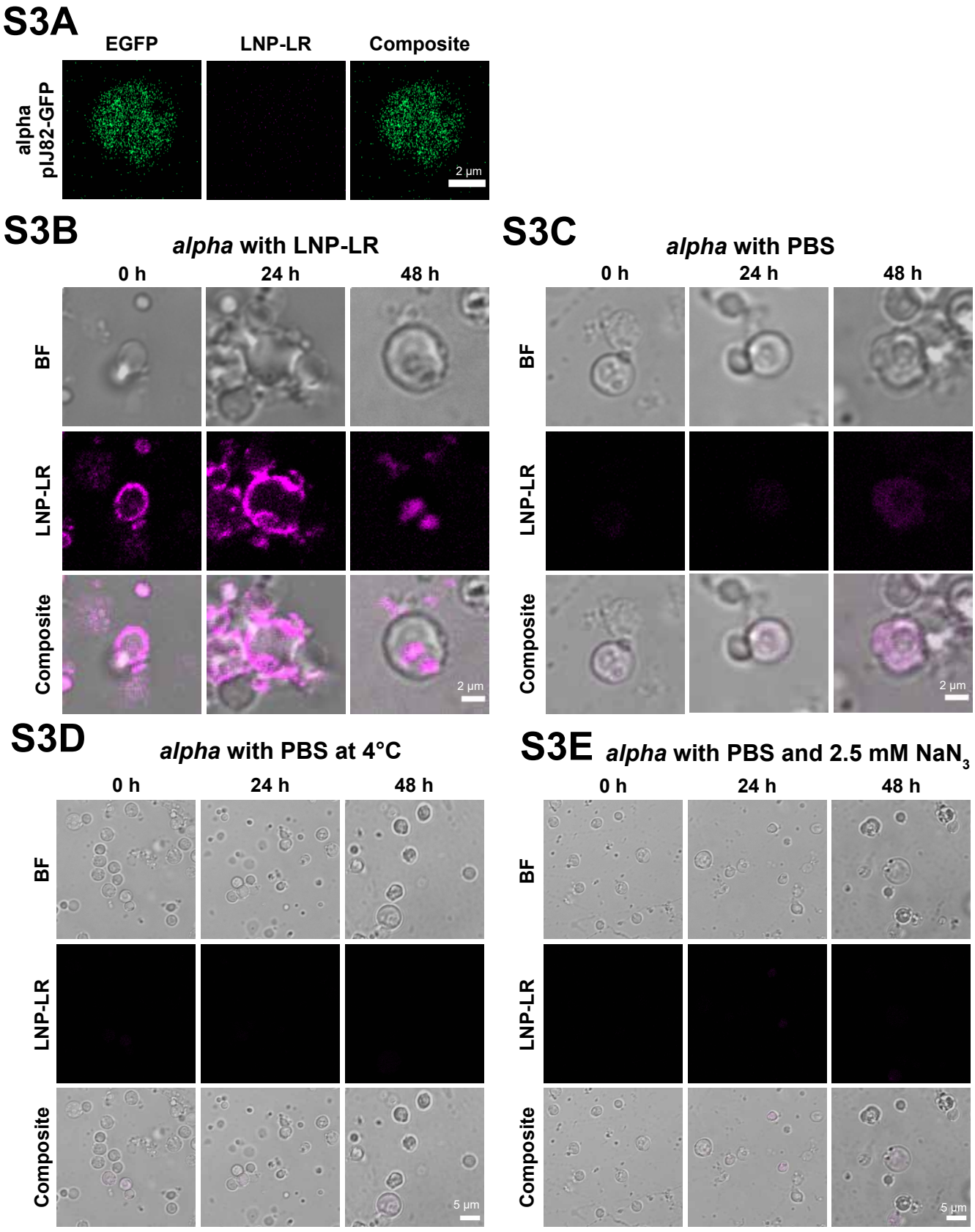

Figure S3. Uptake of LNP-LR by alpha, Related to Figure 3

(A) *alpha* pIJ82-GFP incubated without LNP-LR (LNP-Liss Rhod; magenta) as imaging control.

(B-C) *alpha* incubated with (B) or without (C) LNP-LR showing localization of LNP-LR after 0 h, 24 h and 48 h or examples of autofluorescence, respectively.

(D-E) *alpha* incubated with PBS at 4 degrees (D) or with PBS at 30°C in the presence of 2.5 mM sodium azide (E) as control for fluorescence emission. Images were obtained after 0, 24 and 48 h incubation.

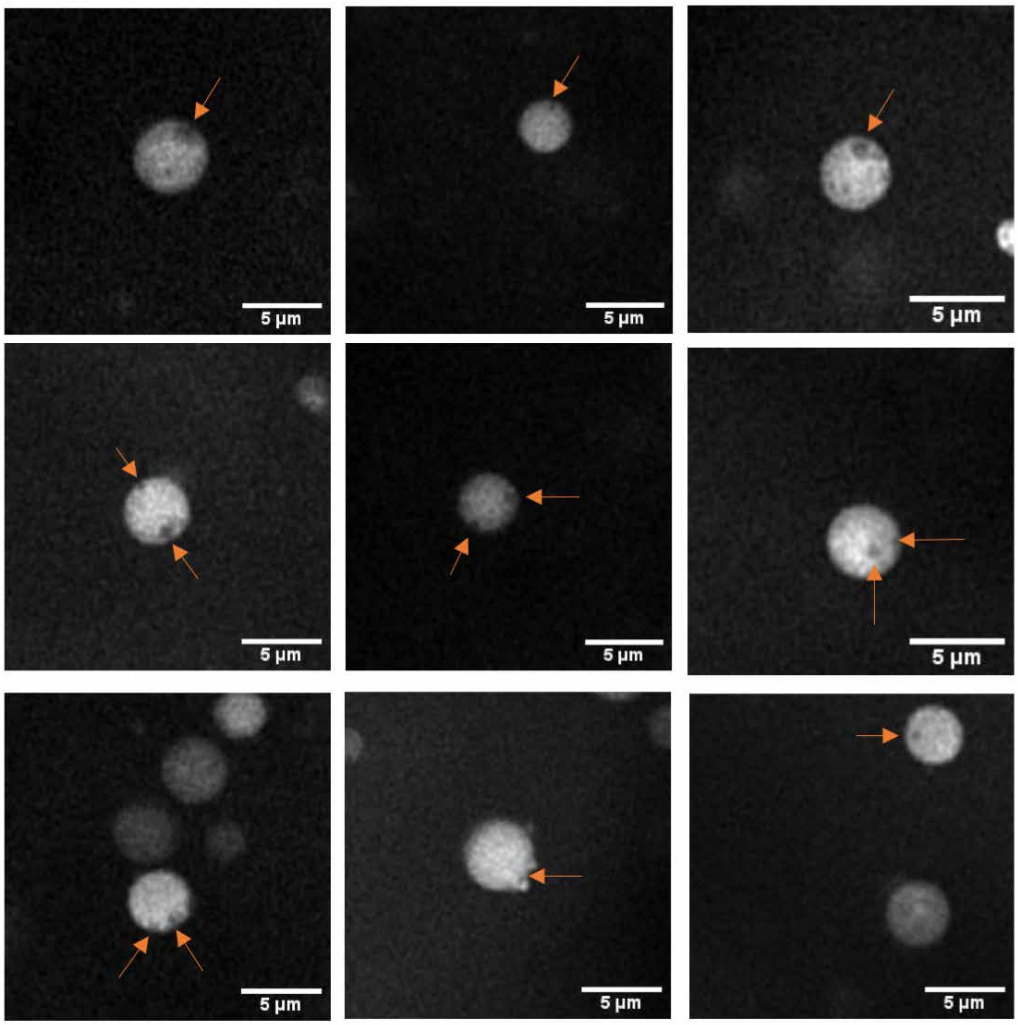

Figure S4. High Resolution Cryo-Fluorescence of L-forms, Related to Figure 4
alpha pIJ82-GFP imaged using cryo-fluorescence microscopy. Putative vesicles are indicated with arrows. Images were captured using the long distance 100x objective.

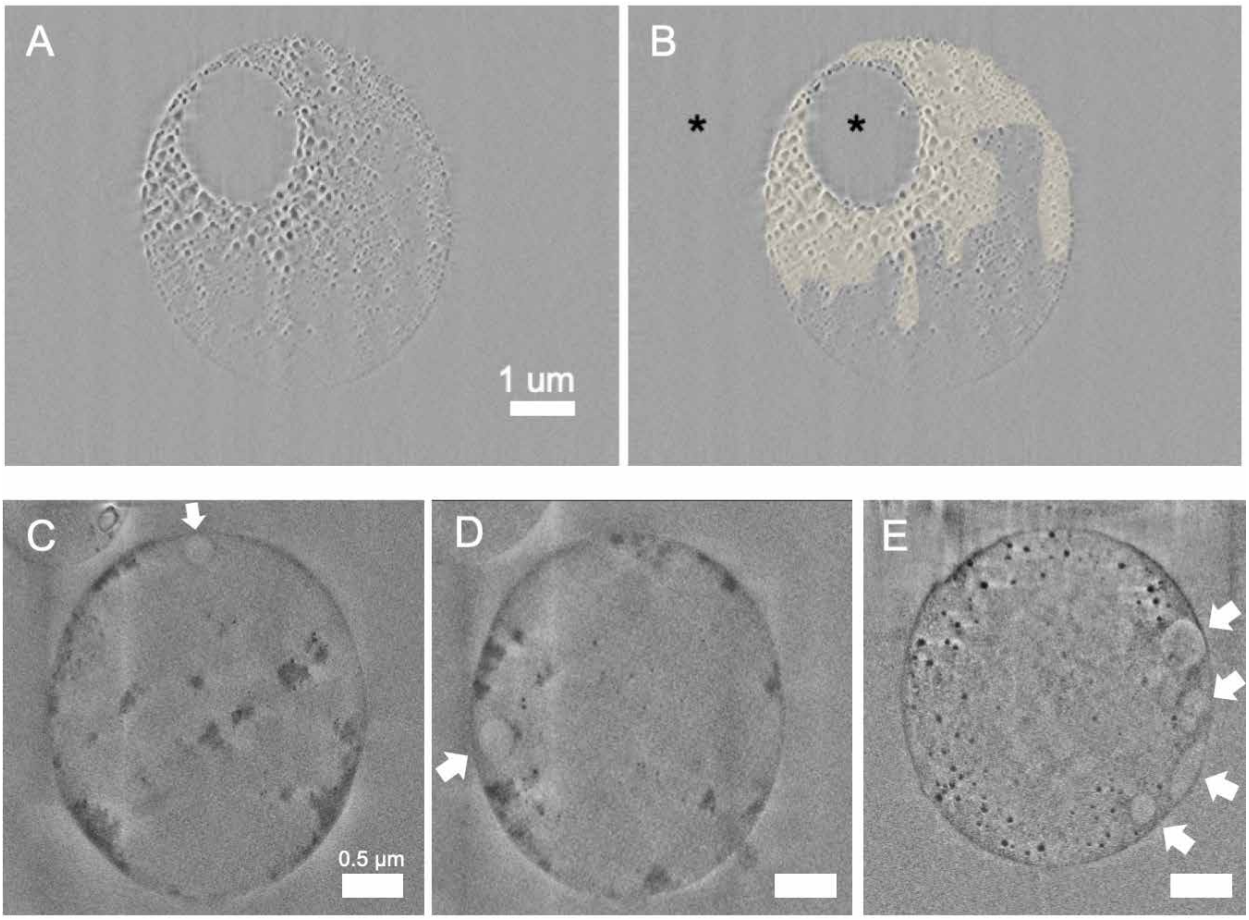

Figure S5. Over-dose experiment of L-form Cell using FIB-SEM, Related to Figure 4

(A-B) FIB-SEM slice of over-dose experiment using *alpha* pIJ82-GFP. The yellow colour in B) indicates areas with distinguished beam damage. The vesicle (black asterisk in the center of the cell) seems to be less to none affected by the dose, similar to the medium outside the cell (black asterisk outside of the cell). The image in Figure 4D is taken before this experiment, and Figure 4E is obtained by summing several slices deeper in the cell after acquiring this image.

(C-E) FIB-SEM slices of two cells (C-D correspond to the cell in Figure 4F and E corresponds to the cell in Figure 4 H-K), white arrows indicate vesicles that line the cell membrane. Scale bar in C-E is 0.5 µm.

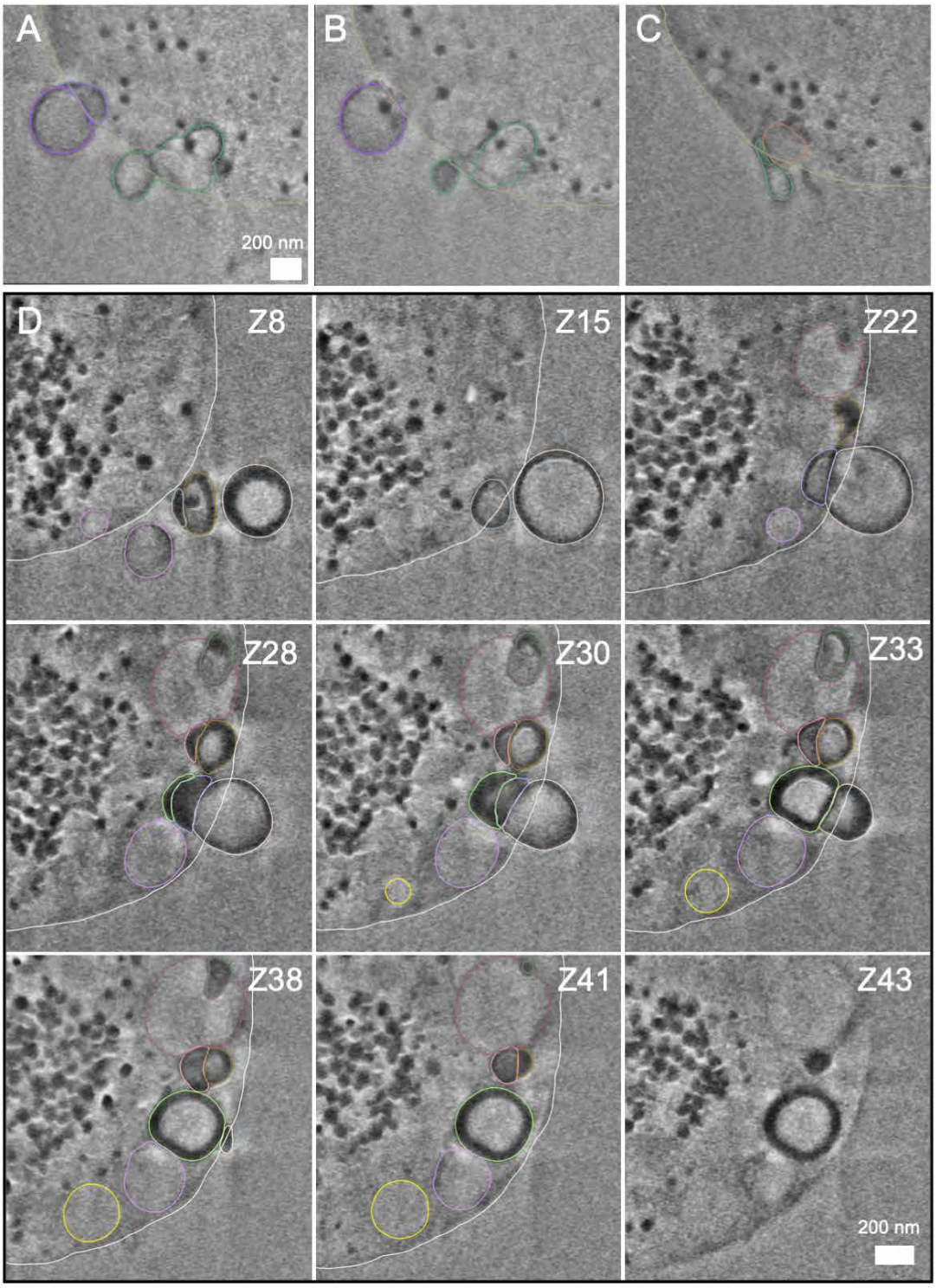

Figure S6. 3D Segmentation of L-form Vesicles, Related to Figure 4

(A-C) FIB-SEM slices corresponding to Figure 4I, Jiv and Ki-iii, respectively. Colours correspond to the segmented colours in Figure 4Kiv. Vesicles that are budding out the cells are connected to other vesicles or are elongated inside the cell. Scale bar = 200 nm. See also Video S2.

(D) FIB-SEM slices corresponding to the cell in Figure 4H. Z-number indicates the slice. Colours indicate individual vesicles. See also Video S3.